**The Raymond and Beverly Sackler Faculty of Exact Sciences**
**Tel Aviv University**

THE SCHOOL OF CHEMISTRY

# Simulations of Exciton Condensation in 2D Twisted Bilayers

Thesis submitted in partial fulfillment of the requirements for the M.Sc. degree in the School of Chemistry, Tel Aviv University

By

**Netanel Bachar Schwartz**

The research work for the thesis has been carried out

under the supervision of

## Dr. Barak Hirshberg

# Acknowledgements

First, I would like to thank my advisor, Dr. Barak Hirshberg for his constant support and guidance throughout this process. A special thanks goes to my research group friends, for all of their support, and for those late night consults. Finally and most importantly I wish to thank my wife, Eden, for always having my back and my dear family for their endless support throughout all my years in academia.

This thesis was written during the Swords of Iron war. As of this date, there are still 133 hostages. I pray for their safe return and will continue to serve in reserves until they do.

# Abstract

Twisted two-dimensional heterostructure bilayers serve as a promising platform for studying high-temperature exciton condensation, due to the high binding energy of indirect excitons and their confinement within the induced moiré potential landscape. In this thesis, we utilize bosonic path integral molecular dynamics to explore exciton condensation in twisted bilayers. We implement an algorithm to calculate the superfluid fraction in path integral molecular dynamics, which acts as a measure for the condensation temperature. Subsequently, we employ this approach to explore the effects of different adjustable parameters that control the moiré landscape on the condensation temperature, such as trap anharmonicity, well-depth, and twist angle. Our simulation results demonstrate that trap anharmonicity has a major effect on the condensation temperature, which highlights the necessity of incorporating it into model Hamiltonians. Also, we observe that increasing the moiré trap depth and raising the relative twist angle between the bilayers leads to a higher superfluid fraction. Our findings provide insights into the design of bilayers that might enable high-temperature exciton condensation in future experiments.

**Keywords**: twisted bilayers, exciton condensation, moiré potential, superfluid fraction, path integral molecular dynamics for bosons.

# Contents

# 1 Introduction & Research Goals

Excitons are quasiparticles that are formed in semiconductors when an excited electron and a positively charged 'hole' form a bound state. Conventional semiconductors typically form direct excitons, characterized by short lifetimes, due to spontaneous recombination [1], and low binding energy, which makes them unstable at high temperatures [2]. However, stacked semiconductor bilayers form indirect excitons, or interlayer excitons, with a spatial separation of the electrons and holes in distinct layers, resulting in prolonged lifetimes of several nanoseconds [3] and high binding energies [4]. Despite being comprised of fermionic electrons and holes, indirect excitons can be approximated as composite bosons for shorter times scales than their lifetime, due to their high binding energy. When bosonic particles are cooled, usually to the micro-Kelvin range, a macroscopic occupation of the single particle ground state is achieved, leading to exciting quantum phenomena, such as Bose-Einstein condensation (BEC) [5]. Recently, twisted two-dimensional (2D) van der Waals bilayer heterostructures have emerged as an exciting platform for exploring exciton condensation at higher temperatures.

Twisted bilayers are created by vertically stacking two monolayers of transition metal dichalcogenides semiconductors (TMDs) with a lattice mismatch or a rotational misalignment between adjacent layers, resulting in a periodic moiré superlattice [6]. The periodically varying moiré pattern provides high symmetry regions that act as local minima or maxima for the bilayer band gap energy. This modulation of the band gap introduces an in-plane periodic potential landscape known as the moiré potential [7, 8], where indirect excitons can be localized [4]. The TMD monolayers are separated by a thin spacer of hexagonal boron nitride (hBN) which decreases the moiré trap depth and suppresses interlayer recombination, thereby further increasing the excitonic lifetime and density. Furthermore, the electron-hole spatial separation produces a permanent repulsive dipole interactions that reduces the formation of exciton complexes at elevated densities [8, 9, 6]. These advantages not only ensure the stability of excitons at elevated temperatures but potentially increase the critical temperature at which they condense, making 2D twisted bilayers an excellent platform for studying high-temperature exciton condensation.

BEC is a quantum state of matter where a macroscopic number of bosons occupy the lowest energy single particle state and their wavefunctions unify into a coherent state, leading to manifestation of quantum phenomena such as superfluidity. Notably, in liquid helium, the superfluidity transition coincides with the formation of the condensate. Superfluidity refers to a state of matter where a substance flows with zero viscosity [10, 5, 11] and can typically be recognized by a reduction in its moment of inertia when subjected to rotation [12, 13, 14, 15, 10]. BEC is most commonly observed in ultracold atoms in the micro-Kelvin regime, thus the potential to observe it in 2D materials is exciting. Due to their lighter mass compared to atoms, excitonic systems can achieve quantum degeneracy at relatively higher temperatures. Consequently, it has been predicted that indirect excitons in TMD bilayers could undergo BEC at high temperatures [16], as evidenced by recent experiments demonstrating high-temperature ($\sim 100$ K) exciton condensation in stacked molybdenum diselenide/tungsten diselenide ($MoSe_2/WSe_2$) heterobilayers [6]. Furthermore, while high-temperature condensation in twisted TMD bilayers has not been reported yet, it has theoretical support [17] and there is experimental evidence of observing interlayer excitons being trapped in moiré potentials [18, 7]. Adjusting the relative twist angle of the bilayers tunes the potential landscape of the moiré excitons, which could help control the condensation temperature.

The relationship between the twist angle and condensation temperature remains uncertain, however, emphasizing the necessity for simulations to achieve a quantitative understanding of BEC formation in twisted bilayers. Recently, computational methods to obtain thermodynamic properties of large bosonic systems were developed, via path integral molecular dynamics (PIMD)[19, 20]. The challenge is then to have a tool for obtaining the condensation temperature from those simulations, which leads to my thesis two main results: implementing the superfluid (SF) fraction, which is a measure for condensation in bosonic PIMD simulations and employ it to investigate the effects of the moiré trap anharmonicity, well-depth and twist angle on the condensation.

Simulations incorporating quantum effects can be conducted using Richard Feynman's path integral formulation of quantum mechanics. The formulation shows that the quantum partition function is isomorphic to a classical partition function of an auxiliary, larger system. The quantum-classical isomorphism, enables the utilization of well-developed

classical simulation methods to obtain quantum expectation values of the original system. In this thesis, molecular dynamics (MD) is selected as the classical method for sampling. Path Integral Molecular Dynamics (PIMD) is a many-body method capable of providing precise estimates of thermodynamic observables for quantum systems at finite temperatures [21, 22]. In PIMD, each quantum particle is mapped to an individual classical ring polymer composed of $P$ beads connected via harmonic springs that depend on temperature [21, 19]. These ring polymers capture the delocalized nature of quantum particles. To perform simulations of exciton condensation, it is crucial to account for bosonic exchange symmetry in the simulations. This requirement necessitates the quantum partition function to include the summation over all possible indistinguishable particle permutations, ensuring accurate representation of symmetric particle exchange, which is consistent with Bose-Einstein statistics. While, traditionally, bosonic PIMD simulations was only feasible for a small number of particles [23], recent studies enabled simulations of thousands of bosons, avoiding permutation enumeration, yet still enforcing the correct statistics [19, 20].

In Path Integral Monte Carlo (PIMC) [21], the condensation temperature is estimated using the superfluid fraction, which is evaluated through permutation sampling [24]. However, in PIMD-B permutations from all configurations are evaluated simultaneously during each MD time step, making it unfeasible to directly extract a precise permutation configuration. To overcome this challenge, we have implemented an algorithm to identify the most probable permutation configuration at each time step during the PIMD-B simulations [25]. The implementation of a stable and reliable SF fraction is one of the goals of this thesis. Another challenge lies in the absence of first-principles Hamiltonians capable of accurately predicting exciton dynamics and thermodynamics in moiré potentials. Previous simulations of exciton condensation rely on heuristic models [13, 26, 9]. These models typically assume a harmonic trap representation for the moiré confinement, with the fundamental frequency adjusted to match experimental observations [8, 3, 18, 13]. In this thesis, we go beyond the harmonic approximation to explore anharmonic confinements and investigate their effect on the condensation. Additionally, we investigate the moiré potential trap of twisted $MoSe_2/WSe_2$ bilayers, whose parameters are experimentally determined [8]. By varying its parameters, we gain a deeper understanding on the effects of well-depth and twist angle of the twisted heterostructure on condensation.

The main objective of this research is to develop a methodology to describe the thermodynamics of exciton condensation in 2D twisted bilayers. This objective is accomplished through the development and testing of the superfluid fraction in PIMD-B as a proxy for condensation and its application to various external potentials. The effects of trap anharmonicity and different moiré potential well-depths and twist angles on the superfluid fraction are compared to a harmonic potential model. Ultimately, these tools will hopefully help design new 2D twisted bilayers with controllable manifestations of fundamental physical and quantum phenomena.

## 1.1 Thesis structure

The thesis is organized as follows: Section 2.1 provides an overview of molecular dynamics simulations as a tool for sampling probability distributions of classical systems at equilibrium. Moving beyond classical simulations to quantum systems, Sections 2.2 and 2.3 discuss the derivation of PIMD for both distinguishable and bosonic particles and explain the process for obtaining thermodynamic observables. Section 2.4 elaborates on the algorithm employed for computing the area estimator utilized in determining the superfluid fraction. Section 3 includes the results and their discussion. Since the development of a new estimator requires careful testing, Section 3.1 benchmarks the superfluid fraction for both ideal and interacting bosons confined in a harmonic trap. Subsequently, in Section 3.2, the superfluid fraction is evaluated for excitons within anharmonic and moiré potential traps. In section 4 the findings are summarized. Finally, section 5 explores current challenges and potential directions for future work. Section 6 presents an appendix that provides supplementary information on various aspects covered throughout the thesis.

# 2 Methodology

## 2.1 Molecular dynamics in a nutshell

Molecular dynamics (MD) is a computational simulation technique for the study of atomic and molecular systems by numerically solving the classical equations of motion for the constituent particles. This technique allows for the analysis of the time-dependent behavior and interactions of atoms and molecules within a given system. MD simulations are widely used for researching structural, thermodynamic, and dynamic properties of materials, such as gases, liquids and solids. The simulations are a valuable tool for comprehending the microscopic behavior of chemical systems, assisting in interpreting experimental observations and predicting material properties [27].

The three key components of MD simulations are: 1) formulating the model that describes interparticle interactions, 2) computing forces based on the model, and 3) employing an algorithm for the integration of the equations of motion. The first two points are usually system-specific with model parameters derived from experimental data or first-principles calculations. The third point provides the dynamics in time, but also determines the ensemble in which the simulation takes place [27]. Many materials are in thermal equilibrium with their surroundings, hence the canonical ensemble predominates in many fields of study. For simulating a system in the canonical ensemble, the addition of a thermostat to the classical equations of motion is essential to ensure the temperature of the system averages to the desired value.

Once an ensemble is defined, MD simulations can also be understood as a tool for sampling probability distributions at equilibrium, assuming the system is ergodic. In this context, ergodicity means exploring all accessible phase space microstates over time. Adequate phase space sampling enables the generation of ensemble averages, for a thermodynamic property, denoted as $a(\mathbf{r})$, through

$$\bar{a} \equiv \lim_{t \to \infty} \frac{1}{t} \int_0^t a(\mathbf{r}(t')) \mathrm{d}t' = \int a(\mathbf{r}) f(\mathbf{r}) \mathrm{d}\mathbf{r} \equiv \langle a \rangle. \tag{1}$$

In Eq. 1, the ensemble average is denoted by $\langle ... \rangle$, $t$ is the total simulation time and $f(\mathbf{r})$ is the equilibrium phase space distribution function which is the probability density of observing a system in the ensemble in a specific point in phase space $\mathbf{r}$. To simplify, let $\mathbf{r} \equiv r = (x, y, z)$ be adopted throughout the thesis.

Studying physical and chemical systems at extremely low temperatures, or of lightweight particles exhibits significant quantum effects, such as zero-point energy, tunneling and interference. However, solving the Schrodinger equation of motion exactly for many-body quantum systems is impossible. Moreover, numerical solutions scale exponentially with system size and demand unreasonable computational resources. This challenge can be addressed by Path Integral Molecular Dynamics (PIMD) simulations which provides an efficient computational method to evaluate thermal expectation values of many-body quantum systems from first-principles.

## 2.2 Path integral molecular dynamics for distinguishable particles

The path integral formulation of quantum mechanics provides a natural framework for evaluating the thermodynamic properties of quantum systems. It reveals that, for distinguishable particles, the quantum partition function of a system is isomorphic to the partition function of a larger classical system consisting of ring polymers, which can be sampled through MD simulations [27]. More specifically, the partition function of the original quantum system can be sampled by representing each quantum particle with a classical ring polymer, composed of $P$ copies of each particle referred to as "beads", which are connected by harmonic springs [28], as we now show.

### 2.2.1 The partition function

For distinguishable particles obeying Boltzmann statistics, the canonical partition function is $Z = Tr\{e^{-\beta \hat{H}}\}$ where $\beta = (k_B T)^{-1}$ is the inverse temperature, $k_B$ is the Boltzmann constant, and $\hat{H}$ is the Hamiltonian of $N$ particles of

mass $m$, given by

$$\hat{H} = \sum_{l=1}^{N} \frac{\hat{p_l}^2}{2m} + U(\hat{r}_1, ..., \hat{r}_N) + \sum_{k \neq l}^{N} V(|\hat{r}_l - \hat{r}_k|). \tag{2}$$

In Eq. 2, $\hat{p}$ denotes the momentum operator, $U(\hat{r}_1, ..., \hat{r}_N)$ is the external potential operator and $V(|\hat{r}_l - \hat{r}_k|)$ is the interparticle interaction potential operator. We chose to focus on potentials that can be described by one- and two-body terms, but the results are more general. The exponent in the trace is the thermal density or Boltzmann operator for distinguishable particles. If we take the trace in the position representation, and by introducing the identity operator $(P-1)$ times, the partition function of the system can then be expressed as,

$$Z = Tr(e^{-\beta \hat{H}}) = \int dR \langle R|e^{-\beta \hat{H}}|R \rangle = \int dR \langle R|(e^{-\tau \hat{H}})^P|R \rangle = \prod_{j=1}^{P} \int dR_j \langle R_j|e^{-\tau \hat{H}}|R_{j+1} \rangle, \tag{3}$$

where $|R_{P+1}\rangle = |R_1\rangle$, $P$ is the number of beads and $\tau = \frac{\beta}{P}$ is the imaginary time step. $R_j = (r_1^j, ..., r_N^j)$ is a notation for the positions of bead $j$ for all $N$ particles. Using the Trotter decomposition of the Boltzmann operator gives rise to the path integral expression for the partition function [29, 27],

$$Z_D = \lim_{P \to \infty} \left(\frac{mP}{2\pi\beta\hbar^2}\right)^{\frac{dNP}{2}} \int e^{-\beta W(R_1, ..., R_P)} dR_1...dR_P, \tag{4}$$

where $d$ is the spatial dimension of the simulation. Eq. 4 shows that the quantum partition function has the same structure as a classical one with an effective potential,

$$W(R_1, ..., R_P) = \sum_{j=1}^{P} \left[ \sum_{l=1}^{N} \frac{1}{2} m\omega_P^2 (r_l^{j+1} - r_l^j)^2 + \frac{1}{P} U(r_1^j, ..., r_N^j) + \frac{1}{P} \sum_{l \neq k}^{N} V(|r_l^j - r_k^j|) \right]. \tag{5}$$

In Eq. 5, $\omega_P = \frac{\sqrt{P}}{\beta\hbar}$ is the harmonic springs frequency between adjacent beads and $r_l^{P+1} = r_l^1$. The prefactor of Eq. 4, comes from integration over the momentum coordinates. The exact result for the partition function is obtained in the limit $P \to \infty$. Practically, a finite number of beads is commonly used and it should be large enough that the thermodynamic observables are converged.
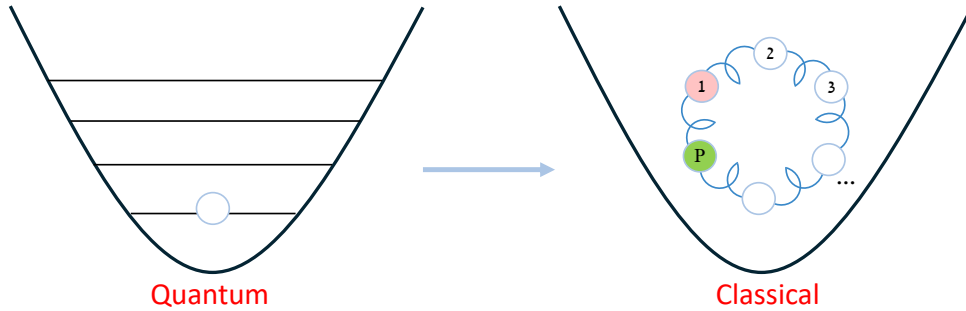


**Figure 1:** Isomorphism between the partition function of a quantum particle in a harmonic external potential and a classical ring polymer

Eq. 5 is equivalent to the classical potential energy of a collection of cyclic ring polymers, composed of $P$ beads each, where every bead is linked to its nearest neighbors by harmonic springs with a frequency of $\omega_P$. Since the spring frequency is directly related to temperature, higher temperatures lead to increased stiffness in the springs. Conversely, at lower temperatures, the springs become more relaxed, allowing for an expansion in size of the polymer rings. In the absence of interactions, the radius of a ring polymer correlates with the thermal deBroglie wavelength. If the thermal deBroglie wavelength is significantly shorter than the interpolymer distance, the system behaves classically. However, when the thermal deBroglie wavelength exceeds the interpolymer distance, quantum effects become significant [29, 21, 30].

### 2.2.2 Sampling PIMD

The potential presented in Eq. 5 represents a classical Hamiltonian suitable for sampling in MD simulations. In this formalism, the notion of 'time' lacks physical significance; with each molecular dynamics time step, a phase space point is generated, contributing to the accumulation of points used for evaluating quantum statistical averages. For simplicity, and without loss of generality, the pair interaction potential is ignored in all subsequent equations. The equations of motion are then expressed as:

$$\dot{r}_l^j = \frac{p_l^j}{m} \qquad\qquad \dot{p}_l^j = -m\omega_P^2(2r_l^j - r_l^{j+1} - r_l^{j-1}) - \frac{1}{P}\frac{\partial U(r_1^j, ..., r_N^j)}{\partial r_l^j} \tag{6}$$

If Eq. 6 is coupled to a proper thermostat, the dynamics will sample the canonical ensemble. The time step in the simulation is chosen depending on, $\omega_{max}$, the highest frequency present in the system. For high frequencies, a shorter time step is used to ensure adequate sampling. A general rule of thumb for choosing the time step is to take one-tenth of the following expression $1/\omega_{max}$.

### 2.2.3 Expectation values from estimators

In PIMD, every thermodynamic observable has a corresponding estimator, from which equilibrium expectation values can be approximated. The path integral expression for an expectation value of an observable $\hat{A}$ comes from $\langle \hat{A} \rangle = \frac{1}{Z}Tr(\hat{A}e^{-\beta\hat{H}})$. For $\hat{A}$ that is position-dependent, performing the trace in the coordinate basis leads to,

$$\langle \hat{A} \rangle = \lim_{P\to\infty} \langle \frac{1}{P}\sum_{j=1}^{P} a(r_1^j, ..., r_N^j) \rangle, \tag{7}$$

where $\langle...\rangle$ indicates the ensemble average over the probability distribution function sampled in the PIMD simulations and $a(r_1^j, ...r_N^j)$ is the corresponding eigenvalue averaged over all beads.

For $\hat{A}$ that depends on the momentum operator, the derivation is slightly more complicated. For instance, the expectation value of the Hamiltonian, a function of both position and momentum is the total internal energy of the system. It's estimator can be derived using a well-known thermodynamic relation, taking the derivative of Eq. 4,

$$E = -\frac{1}{Z}\frac{\partial Z}{\partial \beta} = \lim_{P\to\infty} \langle \epsilon(R_1, ..., R_P) \rangle, \tag{8}$$

where

$$\epsilon(R_1, ..., R_P) = \frac{P}{2\beta} - \sum_{j=1}^{P}\sum_{l=1}^{N}\frac{mP}{2\beta^2\hbar^2}(r_l^{j+1} - r_l^j)^2 + \frac{1}{P}\sum_{j=1}^{P}U(r_1^j, ..., r_N^j). \tag{9}$$

Notice the right hand side of Eq. 9 is consistent with Eq. 7, since it comes from the potential energy which is only a function of position.

Eq. 9, also known as the primitive estimator, suffers from large fluctuations in the two terms that come from the momentum operator, due to their linear dependence on $P$. For simulations that require a large number of beads, the virial theorem for path integrals can be implemented instead, to derive the virial energy estimator,

$$\epsilon(r_l^1, ..., r_l^P) = \frac{1}{P}\sum_{j=1}^{P}\sum_{l=1}^{N}\Big[\frac{1}{2}r_l^j\frac{\partial U}{\partial r_l^j}\Big] + \frac{1}{P}\sum_{j=1}^{P}U(r_1^j, ..., r_N^j). \tag{10}$$

This results in an estimator with a significantly reduced variance and better convergence [27]. In PIMD simulations, it is common practice to observe both the primitive and virial estimators to verify that their thermal averages align, serving as an indicator for potential problems in the simulation.

## 2.3 Path integral molecular dynamics for bosons (PIMD-B)

To perform bosonic simulations, one needs to account for Bose-Einstein statistics of indistinguishable particles. It is a formidable challenge in PIMD, which requires evaluating the trace of the Boltzmann operator over a properly symmetrized basis. This necessitates considering all possible particle permutations within the path integral formulation of the partition function. For a straightforward implementation of PIMD for bosons the number of permutations scales exponentially, $\mathcal{O}(N!)$, making it unfeasible to enumerate all ring polymer configurations in systems containing more than a handful of atoms. The partition function for $N$ bosons is then,

$$Z_B = Tr(e^{-\beta \hat{H}}) = \int dR \frac{1}{N!} \sum_\sigma \langle R|e^{-\beta \hat{H}}|\sigma(R)\rangle \tag{11}$$

where $\sigma$ is one of the $N!$ available permutations [29, 27, 20]. Since the potential operator is invariant under identical particle permutation, its contribution to the path integral expression for bosonic and distinguishable particles is the same. However, a key difference emerges in the contribution due to the kinetic energy operator, which effectively leads to the last bead of a particle $l$ to be connected to the first bead of the permutation of particle $l$, as shown in Fig. 2 for three particles.

When integrating over all beads of all particles in Eq. 11, permutations of the same topology contribute equally to the partition function. Consequently, it is possible to sum over a significantly smaller set of terms. The weight of each term corresponds to the number of distinct permutations that result in the same topology. This reduces the computational cost since not all permutations are summed over, but the number of terms still scales exponentially with $N$ [20].

Hirshberg et al. [19], circumvented the exponential scaling by employing a recurrence relation to sample the bosonic partition function. This method avoids the need to enumerate all permutations and yet ensures accurate thermal expectation values. As mentioned, the potential energy is invariant under particle permutation; therefore, only the kinetic operator term is evaluated in the recurrence relation. This results in a cubic scaling algorithm, $\mathcal{O}(N^3)$, that enables the study of larger bosonic systems of $\sim 100$ bosons.

The bosonic probability distribution function can be expressed with the following recurrence relation,

$$e^{-\beta V_B^{(N)}} = \frac{1}{N} \sum_{k=1}^{N} e^{-\beta(E_N^{(k)} + V_B^{(N-k)})} \tag{12}$$

where

$$E_N^{(k)} = \frac{1}{2} m \omega_P^2 \sum_{l=N-k+1}^{N} \sum_{j=1}^{P} (r_l^{j+1} - r_l^j)^2 \tag{13}$$

and the recursion is terminated by setting $V_B^{(0)} = 0$. In Eq. 13, it is implied that $r_N^{P+1} = r_{N-k+1}^1$ or otherwise $r_l^{P+1} = r_{l+1}^1$. The partition function is then given by,

$$Z_B \sim \int e^{-\beta(V_B^{(N)} + \frac{1}{P} \sum_{j=1}^{P} U(r_1^j,...,r_N^j))} dR_1...dR_P \tag{14}$$

Practically, one needs to evaluate the force acting on each bead due to the $V_B^{(N)}$ potential. Thus, the effective potential on each bead is obtained by taking the logarithm of the recurrence relation,

$$V_B^{(N)} = -\frac{1}{\beta} \ln \left[ \frac{1}{N} \sum_{k=1}^{N} e^{-\beta(E_N^{(k)} + V_B^{(N-k)})} \right] \tag{15}$$

It is worth noting that the effective potential is different than the potential obtained by the sum over all permutations. It includes only the permutations enclosed in a blue square in Fig. 2, but still samples the partition function in an equivalent manner [19, 20]. From Eq. 15 we can also show that the bosonic force is the weighted average of the forces due to those permutations, with the relative weight being the thermal probability of each configuration. Deriving

new estimators from $Z_B$ is essential for obtaining thermodynamic observables in bosonic systems. The estimator for the energy of a bosonic system is presented and derived in [19]. However, the estimator for the potential energy remains the same compared to the distinguishable particle case, as it is invariant under particle permutation.
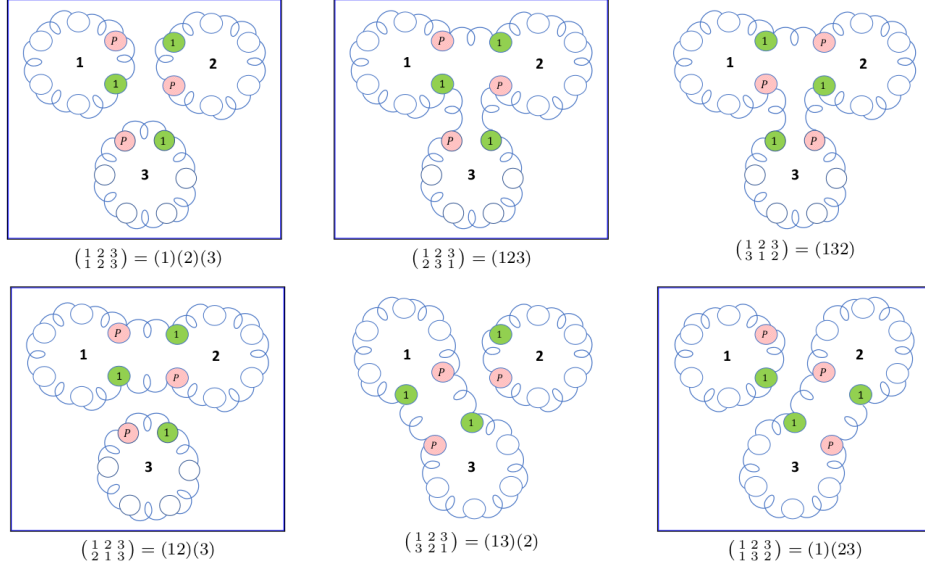


**Figure 2:** Configurations of ring polymers encompassing all possible permutations involving three particles. The permutations that contribute to the potential $V_B^{(N)}$ are marked with blue squares. Source: Reference [20].

In a recent study, a more efficient way of calculating the same recursive potential energy and forces on the beads was presented. This new algorithm reduced the scaling of bosonic simulations from cubic to quadratic, $\mathcal{O}(N^2 + PN)$. This significant improvement enables the execution of simulations involving $\sim 1000$ bosonic particles [20].

## 2.4   Superfluidity in the path integral formalism

With the bosonic PIMD method, we can conduct simulations of excitons in twisted bilayers, assuming they behave like composite bosons. However, a tool to estimate the condensation temperature for BEC formation is required. PIMD is a finite temperature approach that avoids the use of single-particle wavefunctions. Therefore, the typical strategy of analyzing the occupation of the lowest single-particle state is not straightforward to implement. The current community standard relies on the observation that BEC often coincides with superfluidity, as seen in superfluid liquid helium [31]. Consequently, the superfluid fraction usually acts as a proxy for condensation, even in finite systems such as clusters [12, 21].

To derive an expression for the superfluid fraction, consider the following thought experiment: In equilibrium, a regular Newtonian liquid will rotate along with a cylindrical container when slowly rotated. However, a superfluid flows with zero viscosity and would remain stationary. In this latter scenario, less energy would be required to initiate the rotational motion. This is the basic idea behind Andronikashvili's experiment in 1946 [32], which was first theorized by Landau back in 1941 [29, 21, 12]. To describe this phenomenon, Landau proposed the two-fluid model which consists of dividing the fluid into a normal density component and a superfluid density component [31]. These two phases exhibit distinct responses to rotation, characterized by different moments of inertia. Subsequently, the SF fraction can be computed as,

$$\gamma_{sf} = 1 - \frac{I_q}{I_{cl}}. \tag{16}$$

The moment of inertia is evaluated using the following relation: $I = \frac{d\langle L \rangle}{d\omega_0}|_{\omega_0=0}$, where $\omega_0$ is the angular rotation rate, $L$ is the angular momentum, and $I_q$ and $I_{cl}$ represent the quantum and classical moments of inertia, respectively [13]. When the fluid is classical, $I_q = I_{cl}$, resulting in $\gamma = 0$. As for a superfluid, the quantum moment of inertia is reduced with decreasing temperature, leading to $\gamma > 0$.

Within the path integral framework Eq. 16 is estimated [31, 21] as,

$$\gamma_{sf} = \frac{4m^2 \langle A_z^2 \rangle}{\beta \hbar^2 \langle I_{cl} \rangle},$$

(17)

where $A_z$ is the *area estimator* that represents the enclosed area of a permutation by all ring polymers and $I_{cl}$ is the classical moment of inertia of all the beads in the simulation with respect to the center of the external potential and are defined as,

$$A_z = \frac{1}{2} \sum_{l=1}^{N} \sum_{i=j}^{P} (r_l^j \times r_l^{j+1}) \qquad\qquad I_{cl} = m \sum_{l=1}^{N} \sum_{j=1}^{P} (r_l^j \cdot r_l^{j+1}).$$

(18)

Eq. 18 is formulated for two dimensional systems that lies on the $x - y$ plane and thus the $z$ component of the area estimator denotes the total area [31, 6, 10]. However, these equation are adaptable to three dimensions. The derivation of the SF fraction within the path integral formalism is presented in detail in the Appendix section.

The radius of the ring polymers correlates with the thermal wavelength, $\Lambda_\beta = \sqrt{2\pi\beta\lambda_\beta}$, of the quantum particle, where $\lambda_\beta \equiv \frac{\hbar^2}{2m}$. In the high-temperature regime or classical limit, $\Lambda_\beta$ becomes notably smaller than the average interparticle spacing [24]. As a result, bosonic exchange effects diminish in significance, and exchange cycles occur only rarely within the PIMD-B simulation. The mean square area of the ring polymers equals the sum of the mean square areas for each individual ring polymer, denoted as $\langle A^2 \rangle = N \langle a^2 \rangle$. The mean squared area of a single free particle is then denoted as $\langle a^2 \rangle = \frac{(\lambda_\beta \beta)^2}{3}$. As a result, the SF fraction is given by $\gamma_{sf} = \frac{2mN\beta\lambda_\beta}{3I_{cl}}$ and it will be negligible depending on the ratio between the particle's thermal wavelength and the strength of the external potential [21]. At low temperatures, the size of the ring polymers enlarges, reaching a magnitude comparable to the interparticle spacing, thus exchange effects predominate. As a result, ring polymers frequently overlap and merge into longer rings, forming permutation cycles and thereby augmenting their collective mean square area, leading to a larger SF fraction, until it reaches unity [33, 15]. When repulsive interparticle interaction is introduced it causes an increase in the mean interparticle distance, necessitating a significant temperature reduction for particle exchanges to reoccur.

To compute the area estimator, efficient permutation sampling is necessary. However, in PIMD-B, permutations from all topologies contribute simultaneously during each MD time step [19, 20], making it unfeasible to directly extract a precise permutation configuration as in PIMC. To address this challenge, it is necessary to identify the most probable permutation configuration at each MD time step during the PIMD-B simulations [25]. This approach opens up the possibility of evaluating the SF fraction through a permutation sampling bypass.

### 2.4.1 The most probable permutation in PIMD-B

Bosons that are closer than their thermal wavelength are regarded to be within exchange range. As mentioned, in PIMD-B simulations there is no single permutation at every MD time step, unlike in PIMC simulations. It is possible to identify the most probable permutation configuration at each MD time step by comparing and choosing the minimal distance between the first and last bead of particle $i$ and the distance between the last bead of particle $i$ and the first bead of all other $j$ particles, as denoted by, [25].

$$\min \left[ |r_i^{(P)} - r_i^{(1)}|, |r_i^{(P)} - r_j^{(1)}| \right].$$

(19)

In Eq. 19, if the last bead of particle $i$ is closest to its first bead, there is no exchange occurring between particle $i$ and the other particles denoted as $j$. However, if the closest neighbor to the last bead of particle $i$ is the first bead of another particle $j$, it indicates a particle exchange between particles $i$ and $j$, resulting in the last bead of particle $i$ connecting to the first bead of particle $j$. Moreover, if particle $j$ is already undergoing an exchange, the algorithm prevents another particle $i$ from participating in the exchange process. Once all pairs involving the last bead of particle $i$ and the first bead of particle $j$ are identified, they are connected to form the longer ring polymers, and the most probable permutation is determined. This procedure is further detailed in the Appendix.

# 3 Results & Discussion

## 3.1 Implementing the area estimator for the superfluid fraction in PIMD-B

The dimensionless Hamiltonian describing $N$ spinless particles in an external potential $\Delta(\hat{r})$, with a pair interaction of strength $\lambda$ is

$$\hat{H} = -\frac{1}{2}\sum_{k=1}^{N}\nabla_k^2 + \Delta(\hat{r}) + \sum_{k>l}^{N}\frac{\lambda}{|\hat{r}_l - \hat{r}_k|^\alpha}, \qquad (20)$$

where oscillator units are assumed, i.e. the characteristic length is $l_0 = \sqrt{\frac{\hbar}{m\omega}}$, with $\omega$ being the trap frequency, $m$ is the particle's mass, the energy scale is $E = \hbar\omega$ and $\alpha$ is either 1 or 3, corresponding to Coulomb or dipole pair interactions, respectively. In this section, the external potential is represented by the simple harmonic potential, denoted as $\Delta_{harm}(\hat{r}) = \frac{1}{2}\hat{r}^2$ and the Coulomb and dipole pair interactions strength is expressed as $\lambda = El_0$ and $\lambda = El_0^3$, respectively.

All simulation results are obtained for 2D systems with a time step set to 1 fs and a total of $20 \times 10^6$ MD steps, unless mentioned otherwise. In addition, all simulations in this thesis are conducted in the LAMMPS software [34].

### 3.1.1 Estimators convergence

In every PIMD-B simulation, it is essential to carefully select the appropriate time step, number of beads, and duration of the simulation to ensure converged results. The time step for the simulation is chosen to be the highest that conserves the total classical energy of the system. This is determined by executing a PIMD simulation with the thermostat turned off and verifying that the change in total classical energy of the system falls within the range of $\pm 0.1\%$. Next, the number of beads must be chosen so that the corresponding estimator converges. While increasing the number of beads enhances the accuracy of the expectation value, it also prolongs the simulation time. Thus, the number of beads is determined based on the desired accuracy and the convergence of the estimator [27]. Notably, different observables exhibit varying rates of convergence. The simulation duration must be prolonged to adequately sample a representative portion of the phase space, with the precise duration dictated by the measured observable. In practical terms, if the thermal average of the observable remains within an uncertainty range that does not fluctuate with additional simulation time, it is considered adequate.

In Fig. 3, we present the convergence behaviour of the energy, area, and classical moment of inertia estimators with respect to the number of beads in a simulation of $N = 6$ ideal bosons confined under a 2D harmonic trap with a frequency of $\hbar\omega = 3$ meV and electron mass $m_e$. The simulation is conducted at a temperature corresponding to $\beta\hbar\omega = 6$.
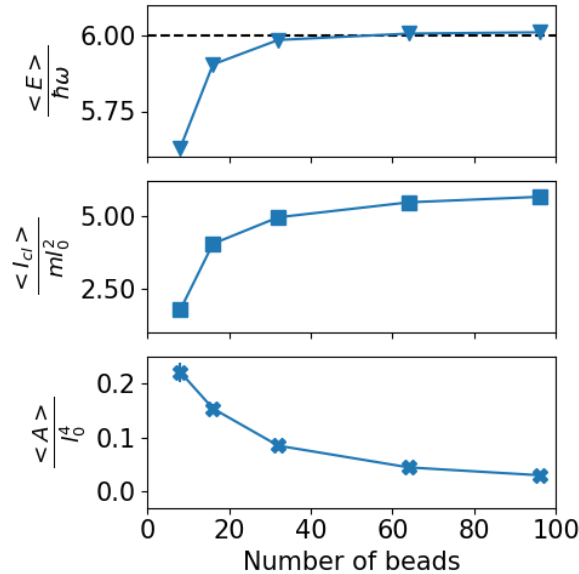
**Figure 3:** Convergence of energy, classical moment of inertia, and area estimators with respect to the number of beads for $N = 6$ ideal bosons confined in a 2D harmonic trap. The black dashed line indicates the ground state energy of 6 ideal bosons in the 2D harmonic trap. Energy, area, and moment of inertia are presented in normalized units.

We find that different estimators exhibit varying rates of convergence. Both the area and classical moment of inertia estimators converge at $P = 96$, whereas the bosonic energy estimator converges between $P = 32 - 64$. At low temperatures, the total energy for bosonic systems closely resembles that of distinguishable particles. Therefore, as Fig. 3 presents, the expected ground state energy for this simulation is $\frac{E}{\hbar\omega} = 6$, derived from $\frac{E}{\hbar\omega} = N(n+1)$ when $n = 0$. This procedure is executed for every simulation in this study, serving as a critical step to ensure the obtained expectation values are both converged and accurate.

### 3.1.2 Benchmark: SF fraction for non-interacting particles in a harmonic trap

To validate the accuracy and consistency of the SF fraction evaluated from PIMD-B simulations, bosonic simulations in the same simple harmonic trap as described above are conducted and compared with their analytical solution. The analytical solution is presented in the Appendix section and can be further explored in [35].

In Fig. 4, each data point represents the average of three independent simulations at inverse temperatures of $\beta\hbar\omega = 6, 5, 4, 3, 2$, and 1. The PIMD-B data aligns with the theoretical prediction across all inverse temperatures, validating the implemented algorithm that identifies the most probable permutation at each MD step.
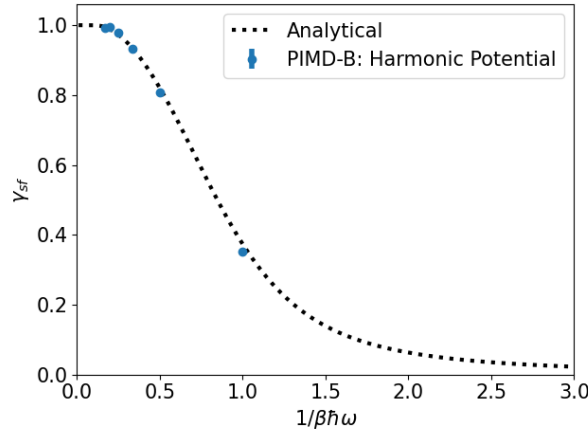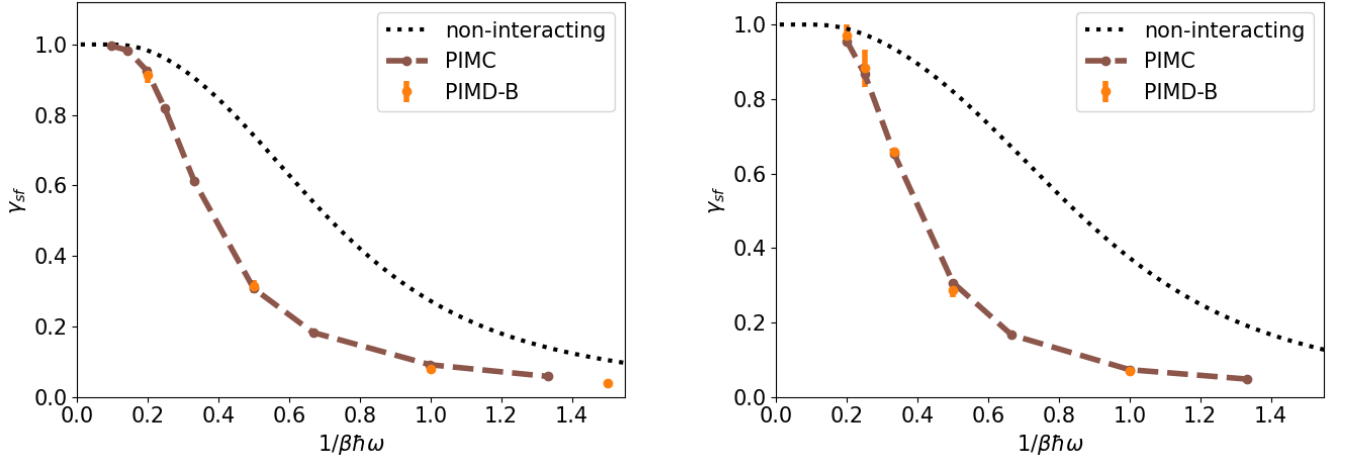


**Figure 4:** Temperature dependence of the SF fraction of $N = 6$ ideal bosons in a 2D harmonic trap. The black line represents the analytical solution, and the blue data points depict the results of PIMD-B simulations. The standard deviation is of the size of the data point measurements.

### 3.1.3 Benchmark: SF fraction for interacting particles

To further validate the SF fraction obtained from PIMD-B simulations, repulsive pair interactions are introduced. Simulations of bosons with mass $m_e$, are confined in a 2D harmonic trap with Coulomb repulsive pair interactions. The fundamental frequency of the harmonic potential is $\hbar\omega = 3$ meV. These simulations are cross-validated against results from PIMC simulations [33].

**Coulomb pair interactions.** The simulations are benchmarked for $N = 4$ and $N = 6$ bosons with a moderate Coulomb interaction coefficient of $\lambda = 3\hbar\omega l_0$. Each data point represents the average of three independent simulations. Presented in Fig. 5, the calculated SF fraction shows excellent agreement with the PIMC results [33]. Notably, a moderate pair repulsion induces a shift in the SF fraction curve towards lower temperatures compared to non-interacting bosons. This can be attributed to the repulsive forces causing a greater separation between the ring polymers, thereby necessitating lower temperatures for the ring polymers to sufficiently approach each other and enable bosonic exchange. Furthermore, the specific number of particles does not significantly influence the qualitative

**Figure 5:** Temperature dependence of the SF fraction of $N = 4$ (left) and $N = 6$ (right) Coulomb pair interacting bosons in a 2D harmonic trap. These simulations are performed at inverse temperatures of $\beta\hbar\omega = 5, 4, 3, 2, 1$ for $N = 4$ and $\beta\hbar\omega = 5, 2, 1$ and $\frac{2}{3}$ for $N = 6$. Results from PIMD-B and PIMC [33] simulations are denoted by orange and brown data points, respectively. The interpolated brown line aids solely in visualization. Additionally, the black dashed line presents the analytical solution for a harmonic potential trap in the absence of pair interactions ($\lambda = 0$).

behavior of the SF fraction. However, the difference between the SF fraction curves for $N = 6$ ideal and interacting ($\lambda = 3\hbar\omega l_0$) bosons is slightly more pronounced compared to the case of $N = 4$. Overall, it shows that in a dilute gas of bosons, the condensation temperature decreases when the particles are more widely dispersed.

## 3.2 Exciton condensation in twisted 2D bilayers

Now that we have successfully implemented the SF fraction in PIMD-B, we can explore how anharmonicity, well-depth, and the periodicity of the moiré potential affect the condensation temperature. Within the twisted moiré superlattice, the band gap modulation between the high symmetry regions gives rise to the moiré potential, where indirect excitons localize. These excitons, with a mean distance between the electron and the hole (Bohr radius) of approximately 1 nm, are significantly smaller than the moiré period. Consequently, the interlayer exciton can be treated as a composite bosonic quasiparticle moving within a varying moiré potential, described by [8],

$$\Delta_{moiré}(r) = 2V \sum_{j=1}^{3} \cos(b_j \cdot r - \psi) \tag{21}$$

where $V > 0$ represents the energy scale of the potential, $b_j$ denotes the moiré reciprocal lattice vectors ($|b| = \frac{2\pi}{a_m}$), $a_m$ is the moiré period [3], and $\psi$ stands for the phase parameter [8]. This potential demonstrates threefold rotational symmetry and ranges between 0 and $6V$.

### 3.2.1 The effects of anharmonicity on the SF fraction

The expression defining the moiré potential, as indicated in Eq. 21, can be fully characterized by two parameters: an energy scale parameter and a shape parameter. This heuristic model is not derived from first-principles but serves as a convenient representation. The phase parameter is fine-tuned to ensure the potential minima is aligned with the high symmetry regions present in the real-space twisted bilayer structure. Usually, in this field of study, it is often assumed that within these regions, the moiré potential traps can be approximated as a harmonic trap, featuring constant quantized energy levels. The constant spacing is then determined from exciton resonances via photo-luminescence measurements, ultimately allowing for the adjustment of the energy scale accordingly. The

harmonic potential model is denoted by,

$$\Delta_{harm}(r) = \frac{1}{2}kr^2 \tag{22}$$

where $k = \frac{16\pi^2 V}{a_m^2}$ and $\omega = \sqrt{\frac{k}{m}}$. However, the exciton spacing measured are not exactly constant, as expected in a harmonic model, and an anharmonic quartic potential could also mimic the moiré trap with similar energy levels. Hence, we introduced a tuned anharmonic potential to examine its effect on condensation. This anharmonic trap is denoted by,

$$\Delta_{anharm}(r) = \lambda r^4 \tag{23}$$

where $\lambda > 0$ is energy scale of the potential. The energy scale parameter in Eq. 23 is tuned utilizing a computational program that numerically solves the time-independent Schrodinger equation for a single-particle. This process involves fine-tuning the energy scale parameter to closely align it with the fundamental optical excitation observed in either an experimental measurement or theoretical results.

Tran et al. conducted a photo-luminescence analysis of the $MoSe_2/WSe_2$ bilayer, revealing multiple interlayer exciton resonance peaks. These peaks arise from the quantized energy levels dictated by the moiré trap. To fit a harmonic model, they average over the observed resonance peaks, leading to an approximate harmonic fundamental energy gap of $22 \pm 2$ and $26.73 \pm 4$ meV for twist angles of 1° and 2°, respectively [8]. To assess the influence of anharmonicity on the SF fraction, we employ the value for a twist angle of 2° and two standard deviations ($2\sigma = 8$ meV) are added and subtracted from the fundamental harmonic energy, resulting in energy values of 18.73 and 34.73 meV. The anharmonic energy scale, $\lambda$, is then tuned to these three fundamental energies. The results are summarized and color-coded in Table 1, and in Fig. 6 the corresponding potentials are presented as a function of position.

| $\hbar\omega$ [meV] | $\lambda\ [\frac{meV}{bohr^4}]$ |
|---|---|
| 34.73 | $5.66e^{-6}$ |
| 26.73 | $2.59e^{-6}$ |
| 18.73 | $3.93e^{-7}$ |

**Table 1:** Fundamental gap energies for the harmonic (blue) and color-coded anharmonic potentials with their corresponding tuned energy parameter.
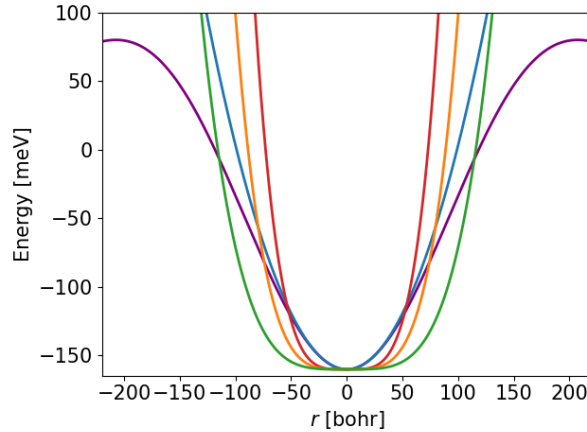


**Figure 6:** The 2D moiré (purple), harmonic approximation to the moiré trap (blue) and three anharmonic potential energies with respect to position at $y = 0$. The fundamental energy of the harmonic potential is $\hbar\omega = 26.73$ meV. The three anharmonic potentials are shown in green, orange, and red, each corresponding to energy scale of $\lambda = 3.93e^{-7}$, $2.59e^{-6}$, and $5.66e^{-6}\ \frac{meV}{bohr^4}$, respectively.
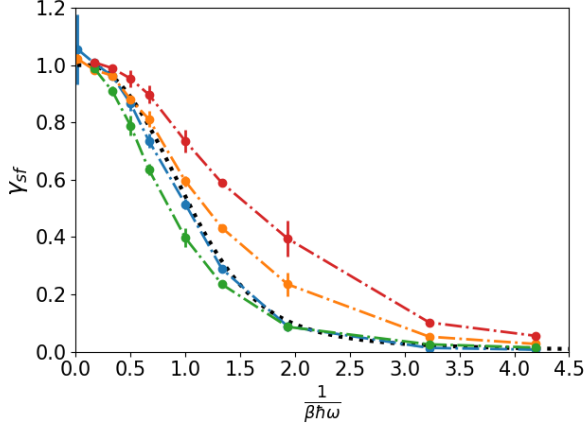
**Harmonic and anharmonic external potentials.** The SF fraction is evaluated in simulations involving $N = 10$ non-interacting excitons with a mass of $0.84m_e$, confined in both harmonic and anharmonic traps. The simulation parameters are outlined in Table 1 and additional simulation parameters are provided in Table 2. Each data point

in Fig. 7 represents the average of five independent simulations.

| $\beta\hbar\omega$ | 6 | 3 | 2 | 1.5 | 1 | 0.75 | 0.5 | 0.31 | 0.23 |
|---|---|---|---|---|---|---|---|---|---|
| $P$ | 64 | 32 | 16 | 16 | 16 | 16 | 12 | 8 | 8 |
| $dt$ [fs] | 0.01 | 0.01 | 0.001 | 0.001 | 0.001 | 0.001 | 0.0001 | 0.0001 | 0.0001 |

**Table 2:** The computational parameters, such as the inverse temperature, number of beads and time steps used for each data point in Fig. 7.



**Figure 7:** Temperature dependence of the SF fraction for $N = 10$ ideal excitons of mass $0.84m_e$ in 2D harmonic and anharmonic potentials. The dashed black curve corresponds to the analytical solution of 10 ideal bosons in a harmonic trap. The units are normalized with $\hbar\omega = 26.73$ meV. The graph is color-coded with Fig. 6 and Table 1.
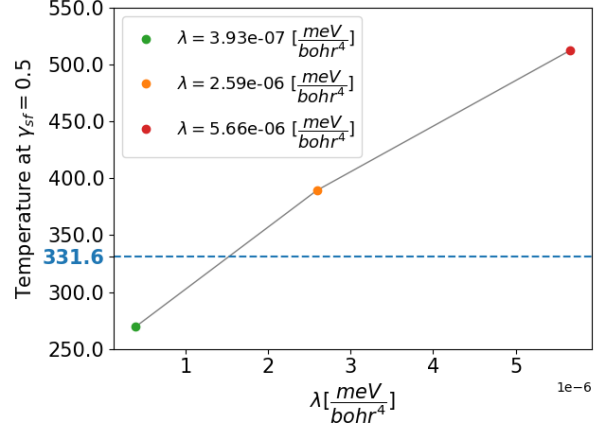
**Figure 8:** The condensation temperature as a function of the anharmonic energy scale. On the y-axis, the condensation temperature of the harmonic simulation is denoted in blue. The graph is color-coded with Fig. 7.

The inflection point of the SF fraction curve occurs at $\gamma_{sf} = 0.5$, which we will use to approximate the condensation temperature. Interestingly, as presented in Fig. 7 and 8, the orange curve notably deviates from the harmonic results, despite sharing the same fundamental energy gap. This deviation results in an increase of 17% in the condensation temperature. At lower temperatures, it closely resembles the outcomes observed in the harmonic curve. Reducing the fundamental energy gap by 8 meV, depicted by the green curve, results in a decrease of 18% in the condensation temperature. Conversely, adding an additional 8 meV into the fundamental energy gap, as shown by the red curve, results in a considerably greater difference in the SF fraction curve with an increase of 50% in the condensation temperature in relation to the harmonic approximation.

As $\lambda$ increases, the anharmonic potential steepens with position, leading to larger spacing between energy levels. At extremely low temperatures, excitons primarily occupy the ground state energy level. However, in potentials with greater spacing between energy levels, the likelihood of excitons transitioning to a higher energy level decreases, resulting in a higher SF fraction for a given temperature. Our simulations show that it is essential to incorporate anharmonicity into model Hamiltonians when interpreting theoretical and experimental measurements, due to their significant impact on the condensation temperature.

### 3.2.2 The effects of moiré trap depth and periodicity on the SF fraction

The unit cell of the moiré potential trap, where indirect excitons localize, is represented by the parallelogram presented in Fig. 9. The selected exciton density, $3 \times 10^{12}$ $cm^{-1}$, exceeds current experimental capabilities by an order of magnitude [6]. Although the simulation runs under periodic boundary conditions across all spatial dimensions, these are not induced. To ensure the excitons remain confined within the periodic boundaries, simulations are exclusively executed at temperatures where thermal fluctuations are smaller than the trap's depth. This requirement must be

met because excitons diffuse at elevated temperatures, and the area estimator, being a local estimator, fails when periodic boundaries are crossed.
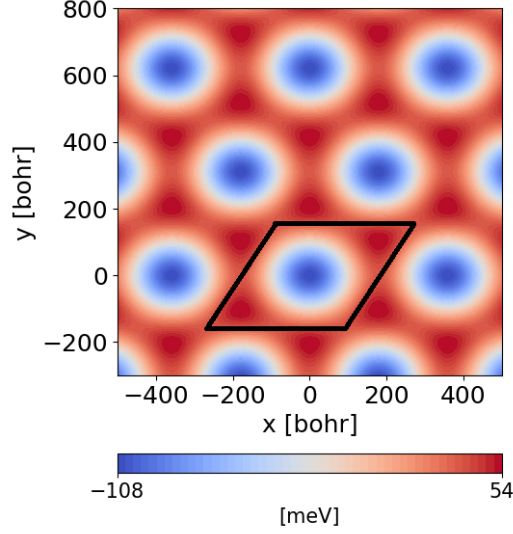


**Figure 9:** The moiré potential landscape of 1° twisted $MoSe_2/WSe_2$, where interlayer excitons are confined within the moiré trap unit-cell delimited by the black parallelogram.
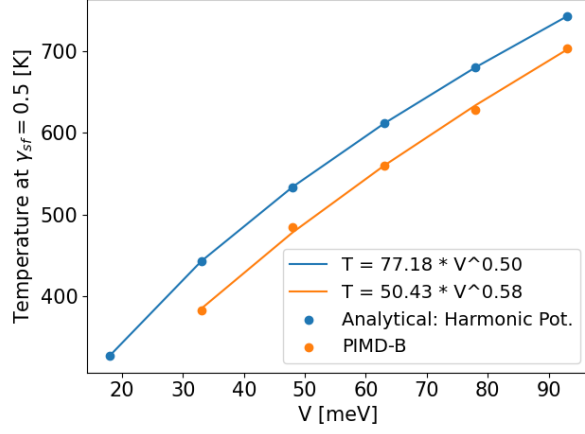
**Moiré well-depth.** The depth of the moiré potential is determined by the interlayer coupling and is estimated to range approximately from 100 to 200 meV in TMD heterobilayers, as predicted by both first-principles calculations and experiments [8]. We want to see the effect of the trap's depth on the condensation temperature. For that, we simulate a twisted $MoSe_2/WSe_2$ bilayer at a fixed 1° twist angle ($a_m = 359$ bohr), involving $N = 10$ non-interacting excitons, each with a mass of $0.84m_e$, confined within moiré traps characterized by hypothetical potential depths of $V = 18, 33, 48, 63, 78, 93$ meV and $\psi = \pi$ [8]. In experiments, reducing the moiré potential depth can be done by incorporating a series of $hBN$ screening layers [3]. The results are presented in Fig. 10.



(a)



(b)
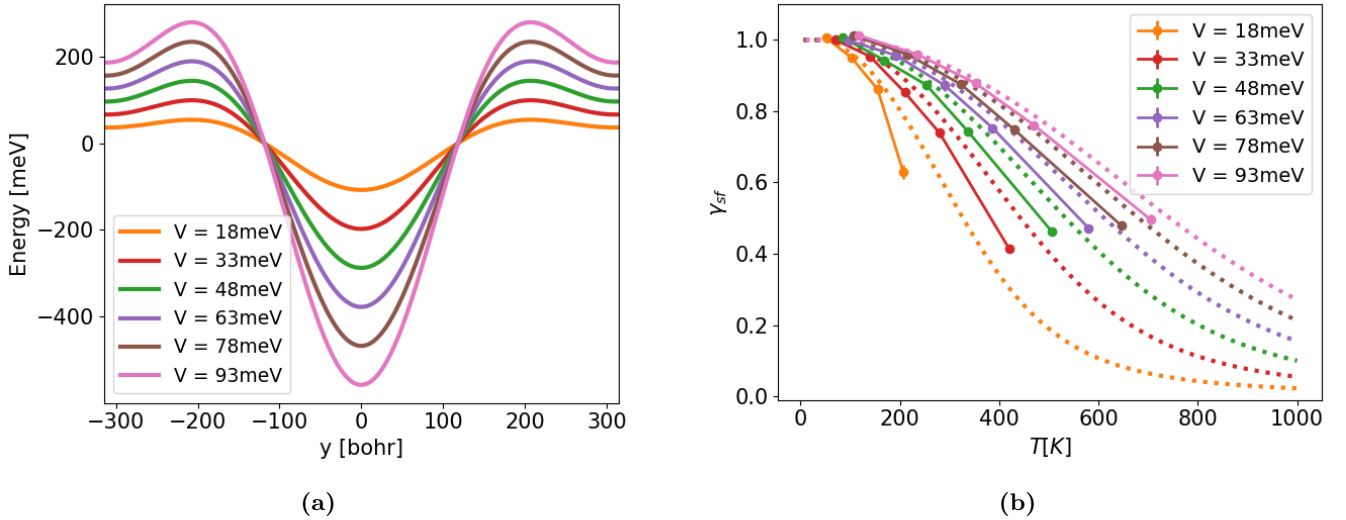
**Figure 10:** a) The moiré potential as a function of position at $x = 0$ for a twisted $MoSe_2/WSe_2$ bilayer with varying well depths, while maintaining the twist angle constant at 1°. b) The SF fraction versus temperature for the color-coded potentials corresponding to Fig. 10a. The dotted color-coded lines correspond to the harmonic potential approximation for each moiré trap.

As presented in Fig. 10b, the SF fraction is greatly affected by the different trap depths shown in Fig. 10a. The deeper the potential, the higher the SF fraction becomes, resulting in a higher condensation temperature. This result is consistent with a theoretical study conducted on interacting bosons trapped in harmonic optical potentials [14].

**Figure 11:** The temperature scaling behavior of the system, governed by a power law, is examined at $\gamma_{sf} = 0.5$ in relation to the depth of the moiré well. Orange points represent results from PIMD-B simulations conducted on the moiré well at varying depths, whereas the blue points depict the corresponding analytical solution for the trap's approximated harmonic well. Solid lines depict the fitted power law functions.

Subsequently, a scaling relationship for the system's temperature at $\gamma_{sf} = 0.5$ is established concerning the depth of the moiré well. The scaling law for the trap's approximated harmonic potential suggests that $T \sim 77\sqrt{V}$. In the other hand, the moiré potential demonstrates a scaling law of $T \sim 50V^{0.58}$. This suggests that the harmonic approximation tends to overestimate the SF fraction and may serve as an upper limit for the condensation temperature when evaluating the moiré potential.

**Moiré twist angle.** The twist angle between adjacent layers introduces an additional degree of freedom, resulting in the emergence and tuning of the moiré pattern in real space. Variances in the relative twist angles between adjacent TMDs monolayers, coupled with the selection of TMDs materials, yield customizable moiré potential landscapes distinguished by differing periodicities and depths.

The correlation between the relative t.a. among adjacent TMD monolayers and the moiré period is inversely proportional [36]. To explore the influence of the twist angle on the condensation temperature, simulations with a t.a of 1° and 2° (corresponding to moiré periods of 359 bohr and 179 bohr, respectively) are conducted. These simulations consider two distinct depths, $V = 18$ and $63$ meV, and involve $N = 10$ non-interacting excitons per unit cell. The results are presented in Fig. 12.
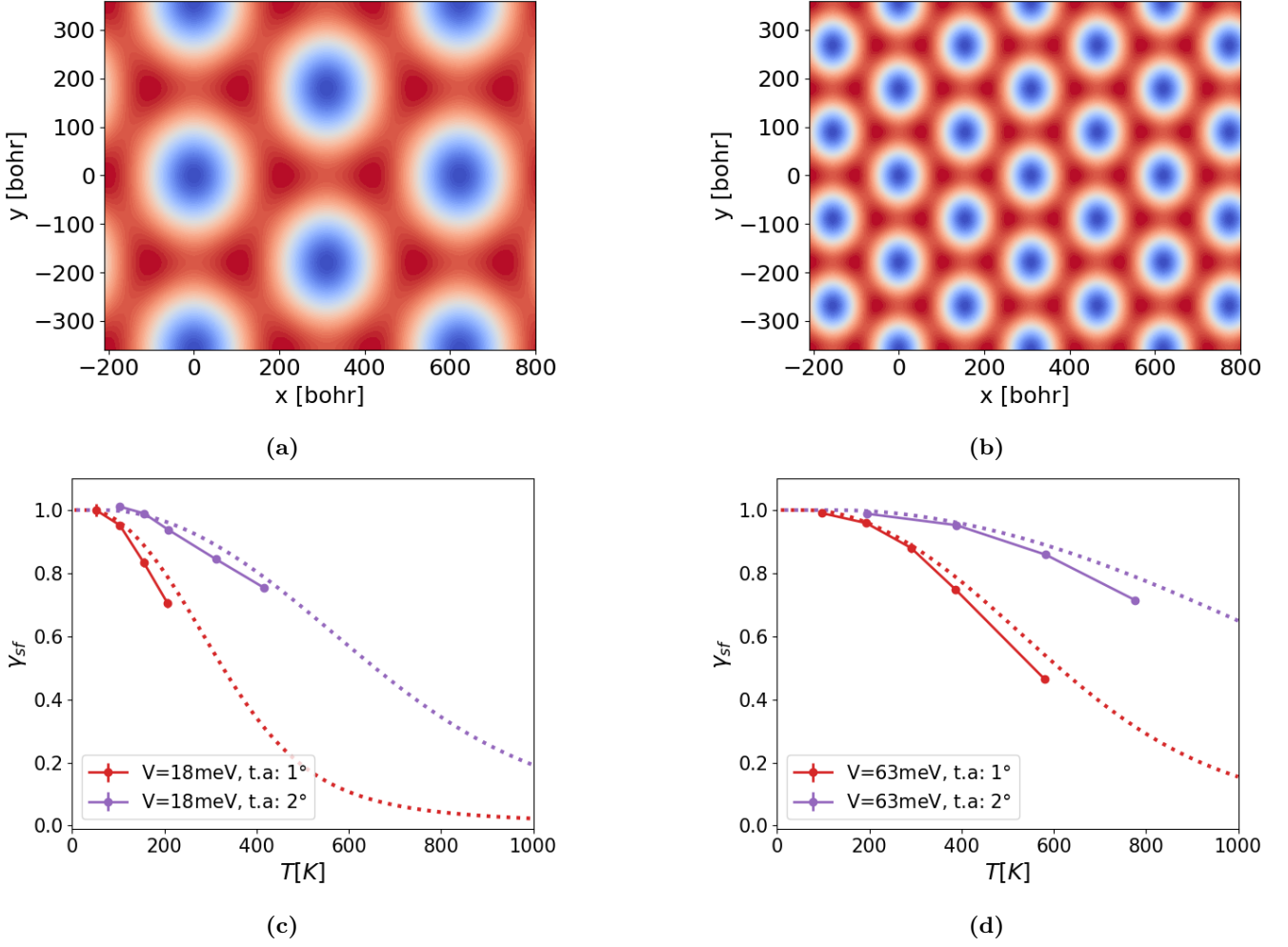
**Figure 12:** a,b) The 2D moiré potentials heat-map corresponding to twist angles of 1° (left) and 2° (right). c,d) SF fraction plotted against temperature for twist angles of 1° and 2°, and potential depths of 18 meV (left) and 63 meV (right). The dotted color-coded lines represent the harmonic potential approximations for each moiré trap.

In Fig. 12, we qualitatively examine the influence of the moiré potential on the SF fraction across varying t.a. and depths. The selected twist angles of 1° and 2° in accordance with the experiment conducted by Tran et al [8]. Our results reveal a consistent pattern: as the twist angle increases, regardless of the trap's depth, there is a notable enhancement in the SF fraction. This trend arises from the fact that an increased twist angle effectively reduces the moiré period, thereby steepening the trap (at a given depth), resulting in an elevation of the condensation temperature. These observations underscore the significant impact of twist angle adjustments on the characteristics of moiré systems, offering potential avenues for manipulating the condensation temperature.

# 4 Summary & Conclusions

Because of their light masses and high binding energies, excitons in 2D twisted bilayer semiconductors are expected to condense at higher temperatures. The periodically varying moiré pattern of rotationally misaligned bilayers provides high symmetry regions that induce a moiré potential, where indirect excitons are localized. In this thesis, through first-principle calculations, we developed a methodology to describe the thermodynamics of indirect exciton condensation in the presence of a tunable moiré potential.

In the path integral formalism, the condensation temperature is estimated using the superfluid fraction. In PIMD-B, permutations from all topologies are evaluated simultaneously, making it unfeasible to directly extract a precise permutation configuration. We overcame this challenge by implementing an algorithm that identifies the most probable permutation at each MD time step. By validating our algorithm for evaluating the superfluid fraction of ideal and interacting trapped bosons, we have demonstrated its accuracy and reliability in various external potential systems.

Our findings highlight the importance of external potentials in theoretical models of exciton condensation, as they significantly influence the thermodynamic properties. Previous simulations of exciton condensation relied on heuristic models of harmonic traps representing moiré confinements. We went beyond the harmonic approximation and explored the effects of anharmonic confinements, different moiré potential well-depths and twist angles on the condensation temperature. By considering anharmonic potentials, we found that the condensation temperature increases by about 20% for a quartic potential with the same fundamental energy as the harmonic approximation. Furthermore, our findings demonstrate a clear qualitative association between a higher twist angle and a deeper moiré trap with an increase in the superfluid fraction. These observations highlight how adjusting the twist angle can greatly affect the properties of moiré systems, providing potential ways to control condensation.

In conclusion, this work lays a computational framework capable of offering insights that could potentially help the observation of high-temperature exciton condensation. This theoretical understanding will allow the prediction of new 2D materials with controllable fundamental physical and quantum phenomena.

# 5 Future Work & Challenges

## 5.1 SF fraction for strong dipole repulsive interacting particles

**Strong dipole pair interactions.** While evaluating the SF fraction approach performs effectively in PIMD-B simulations under ideal and moderate Coulomb interactions, challenges arise when simulating bosons with moderate to strong repulsive dipole pair interactions. As presented in Fig. 13, this problem is shown in our simulations involving $N = 4$ bosons of mass $m_e$ and strong repulsive dipole pair interaction coefficient of $\lambda = 3\hbar\omega l_0^3$. Each data point represents the average of three independent simulations, benchmarked against PIMC results [35].
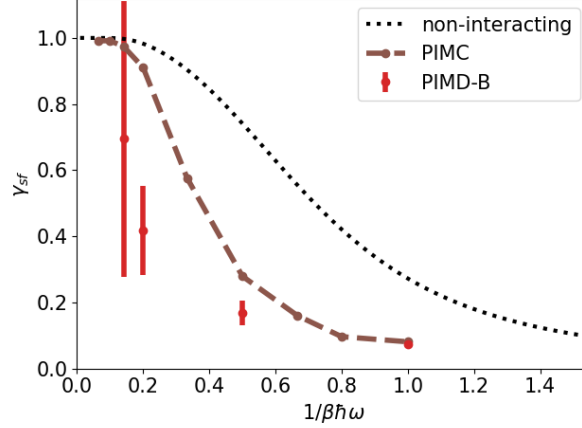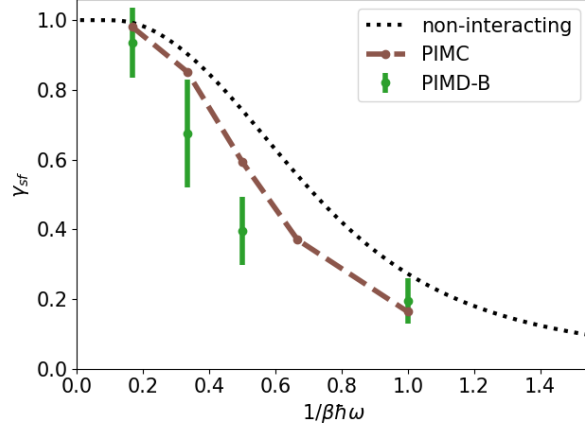


**Figure 13:** Temperature dependence of the SF fraction in bosonic simulations with a dipole pair interaction strength of $\lambda = 3\hbar\omega l_0^3$ in a 2D harmonic trap. These simulations are conducted at inverse temperatures of $\beta\hbar\omega = 7, 5, 2$, and 1. Results from PIMD-B and PIMC simulations [35] are represented by red and brown data points, respectively. The interpolated brown line aid in visualization. Additionally, the black dashed line presents the analytical solution in the absence of pair interactions ($\lambda = 0$).

At low temperatures, the SF fraction obtained from our simulations demonstrates poor agreement with the PIMC results [35]. As particle repulsion strengthens, the interparticle distance increases beyond their thermal wavelength, causing our algorithm, which identifies the most probable permutation, to fail, as it only manages to identify the distinguishable permutation. For temperatures ranging between $2 < \beta\hbar\omega < 6$, PIMC results suggest that the predominant permutation is not the identity permutation, but another permutation involving particle exchange, resulting in a higher value for the SF fraction. Consequently, it is necessary to reassess the implementation and limitations of the algorithm used to identify the most probable permutation.

### 5.1.1 Limits of the most probable permutation algorithm

It is speculated that the most probable permutation is not accurately selected for strong repulsive systems. To understand the limitations of this algorithm, two approaches are employed. Firstly, simulations are conducted for weak dipole pair interactions such as $\lambda = 0.3\hbar\omega l_0^3$ and $0.1\hbar\omega l_0^3$. Secondly, simulations involving distinguishable particles with identical simulation parameters are executed. The former reveals that the algorithm loses its validity under moderate to strong repulsion between ring polymers. Meanwhile, the latter approach will further validate the speculation by demonstrating that the issue lies not in the implementation of the code, but rather in the selection of the most probable permutation. Both approaches are compared to PIMC results.

**Interaction strength.** The simulations of weak pair interactions utilize identical parameters to those in Fig. 13, with the exception of the pair interaction strength. As presented in Fig. 14, with a weak repulsion strength, there appears to be an improved, though still inadequate fit to the PIMC results. The standard deviation remains large, but qualitatively, the agreement is better.

**Figure 14:** Temperature dependence of the SF fraction of $N = 4$ weak dipole pair interacting bosons ($\lambda = 0.3\hbar\omega l_0^3$) in a 2D harmonic trap. These simulations are performed at inverse temperatures of $\beta\hbar\omega = 5, 3, 2$ and 1. Results from PIMD-B and PIMC simulations [35] are denoted by green and brown data points, respectively.

Specifically, for even weaker interaction strengths, such as $\lambda = 0.1\hbar\omega l_0^3$, the PIMD-B outcomes closely converge to the PIMC results, as evidenced for both $\beta\hbar\omega = 2$ and 5 in Table 3. The standard deviation of all PIMC results in this section is on the order of $10^{-5}$. The energy, area, and moment of inertia in Tables 3, 4, and 5 are normalized units of $\frac{\langle E \rangle}{\hbar\omega}$, $\frac{\langle A^2 \rangle}{l_0^4}$ and $\frac{\langle I_{cl} \rangle}{ml_0^2}$, respectively.

|  | PIMD-B | PIMC | error [%] |
|---|---|---|---|
| $A_z^2$ | $2.14 \pm 0.70$ | 2.32 | 8 |
| $I_{cl}$ | $7.08 \pm 0.24$ | 7.11 | 1 |
| $\gamma_{sf}$ | $0.61 \pm 0.22$ | 0.65 | 6 |

a) $\beta\hbar\omega = 2$ and $\lambda = 0.1\hbar\omega l_0^3$

|  | PIMD-B | PIMC | error [%] |
|---|---|---|---|
| $A_z^2$ | $7.05 \pm 0.44$ | 7.38 | 4 |
| $I_{cl}$ | $6.00 \pm 0.02$ | 6.26 | 4 |
| $\gamma_{sf}$ | $0.94 \pm 0.06$ | 0.94 | 0 |

d) $\beta\hbar\omega = 5$ and $\lambda = 0.1\hbar\omega l_0^3$

**Table 3:** A comparison between the mean values for the area, classical moment of inertia, and SF fraction derived from PIMD-B simulations versus the corresponding PIMC results at different inverse temperatures.

In the strong repulsion limit of $\lambda = 3\hbar\omega l_0^3$ and inverse temperature of $\beta\hbar\omega = 5$, both the energy and classical moment of inertia estimators closely align with the PIMC results, as demonstrated in Table 4. These estimators rely on the dynamics of the simulation. However, the area estimator notably deviates by 58% from the PIMC result. This specific estimator depends on the most probable permutation obtained at each MD step. Consequently, it can be inferred that identifying the most probable permutation algorithm requires a generalization in order to incorporate the correct exchange cycles occurring within strong repulsive systems.

|  | PIMD-B | PIMC | error [%] |
|---|---|---|---|
| $\langle E \rangle$ | $11.12 \pm 0.06$ | 11.00 | 1 |
| $\langle A_z^2 \rangle$ | $5.72 \pm 1.01$ | 13.67 | 58 |
| $\langle I_{cl} \rangle$ | $12.01 \pm 0.04$ | 12.17 | 1 |

**Table 4:** For an interaction strength of $3\hbar\omega l_0^3$ the averages of the energy, area and the classical moment of inertia obtained from PIMD-B simulations are compared to PIMC results. The area estimator error is highlighted in red due to its substantial deviation from the expected result.

**Code implementation.** To rule out any potential coding or pair interaction implementation issues, we compare results using the same parameters as before but with distinguishable particles, applying Boltzmann statistics rather than Bose statistics. We conduct PIMD simulations involving $N = 4$ distinguishable particles under a 2D harmonic potential and strong repulsive dipole interaction of $\lambda = 3\hbar\omega l_0^3$. These results are then directly compared to the PIMC results obtained by T. Dornheim.

| $\beta\hbar\omega$ | 0.75 | 1 | 2 | 3 | 5 |
|---|---|---|---|---|---|
| $\langle E \rangle$ | 16.927±0.036 | 14.853±0.015 | 12.1976±0.0087 | 11.5700±0.0084 | 11.217±0.020 |
| $\langle A_z^2 \rangle$ | 0.1717±0.00068 | 0.2944±0.0011 | 0.995±0.011 | 1.777±0.019 | 3.361±0.047 |
| $\langle I_{cl} \rangle$ | 17.878±0.041 | 15.8177±0.0065 | 13.1629±0.0093 | 12.5007±0.0063 | 12.074±0.012 |
| $\gamma_{sf}$ | 0.051±0.00025 | 0.074±0.00028 | 0.151±0.0018 | 0.189±0.0020 | 0.222±0.0030 |

| $\beta\hbar\omega$ | 0.75 | 1 | 2 | 3 | 5 |
|---|---|---|---|---|---|
| $\langle E \rangle$ | 16.937 | 14.839 | 12.189 | 11.586 | 11.292 |
| $\langle A_z^2 \rangle$ | 0.1777 | 0.3054 | 1.0236 | 1.8918 | 3.7153 |
| $\langle I_{cl} \rangle$ | 17.9148 | 15.8587 | 13.2734 | 12.6882 | 12.4101 |
| $\gamma_{sf}$ | 0.053 | 0.077 | 0.150 | 0.198 | 0.239 |

**Table 5:** A comparison between the energy, squared area, classical moment of inertia, and SF fraction thermal averages obtained from PIMD simulations (top table) and PIMC results (bottom table) directly obtained from T. Dornheim.

Our simulations demonstrate good agreement (less than $\sim 5\%$) across all estimators, indicating an accurate representation of the dipole system for distinguishable particles and its implementation. This consistency confirms that the issue lies within the area estimator evaluated in the bosonic simulations, which is directly connected to the way exchange cycles are constructed. This suggests that the sampling of the most probable permutation is inaccurately evaluated in strong repulsive systems, leading to non-ergodic permutation sampling. Consequently, exchange cycles that do occur in practice are not taken into consideration for moderate or strong repulsive interactions.

Notably, the area estimator does not always vanish for finite distinguishable systems. While the average area tends to zero due to both negative and positive contributions of each configuration, averaging over $A_z^2$ prevents these finite contributions from canceling out. This phenomenon is not tied to superfluidity but rather to the change of the moment of inertia of the Boltzmann system due to quantum effects and is not further explored in this thesis.

### 5.1.2 Possible improvements for the most probable permutation algorithm

**Particle shuffling.** Similar outcomes to PIMC can be replicated when simulating distinguishable particles with strong repulsive pair interactions. This outcome arises from the fact that in PIMD, only the identity permutation is dynamically sampled at every MD step. However, when dealing with bosons, even though we correctly sample the partition function, certain permutations are omitted from the dynamical process. While we do sample all topologies, not all permutations are taken into consideration, resulting in faster simulations. To evaluate more precisely the area estimator one needs to have all permutation sampled dynamically. To address this, it is necessary to implement a shuffling technique (as previously done by Chang Woo et al [25]) between all particles that allows for the effective sampling of all possible permutations, ultimately having ergodic simulations.

**Permutation probability.** The current algorithm identifies the most probable permutation, although alternative permutations may also be valid. Introducing a mechanism capable of assigning a weight to each potential permutation could ultimately lead to the derivation of a weighted area estimator. Fortunately, these weights can already be obtained from the new recursive algorithm proposed for bosonic simulations [20], which calculates the "connection probabilities" indicating whether bead $P$ of particle $i$ is linked to bead 1 of particle $i'$ when $i, i' \in \{1, ..., N\}$. In essence, the most probable permutation would receive a higher weight, while other permutations with larger areas would have smaller weighted values since these are less probable. This results in a weighted area estimator, where the probabilities of different permutations are taken into consideration.

## 5.2 Periodic systems

To evaluate the superfluid fraction in a periodic system the winding estimator must be computed. The winding number is a quantity that indicates the number of times the ring polymers wind around the periodic boundary conditions. Once this number is known for every MD time step, the superfluid fraction can then be estimated by,

$$\gamma_{sf} = \frac{m\langle \mathcal{W}^2 \rangle L^2}{\hbar^2 \beta N} \tag{24}$$

where the winding number, denoted as $\mathcal{W}$, is defined as,

$$\mathcal{W} = \frac{1}{L} \sum_{l=1}^{N} \sum_{j=1}^{P} (r_l^j - r_l^{j+1}) \tag{25}$$

and $L$ represents the length of the unit cell. It's important to note that the winding number is quantized in units of the unit cell length. Mainly due to exchange effects and low temperatures the ring polymers become incredibly large and thus increasing the winding number.

The moiré potential is periodic, however the area estimator can only be used if the simulation of ideal bosons is limited to temperatures below the threshold when diffusion starts. The specific temperature at which this restriction applies depends on both the depth and period of the moiré potential [21, 15]. Consequently, as presented in Fig. 10 and 12, simulations were halted below that temperature threshold. Hence, to accurately estimate the SF fraction for this periodic system at higher temperatures, the winding estimator needs to be evaluated instead.

## 5.3 First-principles methodology to describe exciton condensation

The main goal of this thesis can be generalized by developing a method for simulating exciton condensation in twisted bilayer systems, calculated solely using first-principles approaches. This can be achieved by combining stochastic electronic structure methods with PIMD-B simulations. Traditionally, the band gap of twisted bilayers has been calculated from their pristine (untwisted) structures. Then, through analysis of how the band gap varies across different stacking configurations, one can define the moiré potential to describe the fully twisted structure. However, a recent method developed by Dr. Vojtech Velcek's group at UCSB allows for consideration of the entire bilayer heterostructure in the twisted system. To bridge these different simulation approaches, model Hamiltonians can be built based on this recent electronic structure calculations method and used in our path integral simulations. Developing a first-principles approach to describe exciton condensation could significantly aid in guiding future experiments and advancing the realization of exciton condensation in twisted bilayers.

# References

[1] Alexander High and Arthur et al/ Gossard. "Spontaneous coherence in a cold exciton gas." In: *Nature* 483 (Mar. 2012), pp. 584–8. DOI: 10.1038/nature10903.

[2] Kha Tran and Akshay et al. Singh. "Moiré and beyond in transition metal dichalcogenide twisted bilayers." In: *2D Materials* 8 (Dec. 2020). DOI: 10.1088/2053-1583/abd3e7.

[3] Suman Chatterjee and Kausik et al. Majumdar. "Harmonic to anharmonic tuning of moiré potential leading to unconventional Stark effect and giant dipolar repulsion in WS2/WSe2 heterobilayer." In: *Nature Communications* 14 (Aug. 2023). DOI: 10.1038/s41467-023-40329-3.

[4] Thomas Mueller and Ermin Malic. "Exciton physics and device application of two-dimensional transition metal dichalcogenide semiconductors." In: *npj 2D Materials and Applications* 2 (Dec. 2018). DOI: 10.1038/s41699-018-0074-2.

[5] J Eisenstein and A. Macdonald. "Bose-Einstein Condensation of Excitons in Bilayer Electron Systems." In: *Nature* 432 (Mar. 2005), pp. 691–4. DOI: 10.1038/nature03081.

[6] Z et al. Wang. "Evidence of high-temperature exciton condensation in two-dimensional atomic double layers." In: *Nature* 574 (0 Oct. 2019), pp. 76–80. DOI: 10.1038/s41586-019-1591-7.

[7] Alexander Tartakovskii. "Excitons in 2D heterostructures." In: *Nature Reviews Physics* 2 (Dec. 2019), pp. 1–2. DOI: 10.1038/s42254-019-0136-1.

[8] Tran K. and Moody G. et al. "Evidence for moiré excitons in van der Waals heterostructures." In: *Nature* 567 (2019), pp. 71–75. DOI: doi:10.1038/s41586-019-0975-z.

[9] Yu. E. Lozovik and M. Willander et al. "Structural properties of the condensate in two-dimensional mesoscopic systems of strongly correlated excitons." In: *Jetp Lett.* 79 (2004), pp. 473–478. DOI: doi.org/10.1134/1.1780555.

[10] T. Dornheim, A. Filinov, and M. Bonitz. "Superfluidity of strongly correlated bosons in two- and three-dimensional traps." In: *Phys. Rev. B* 91 (5 Feb. 2015), p. 054503. DOI: 10.1103/PhysRevB.91.054503.

[11] G. Chauveau and S. Stringari et al. "Superfluid Fraction in an Interacting Spatially Modulated Bose-Einstein Condensate." In: *Phys. Rev. Lett.* 130 (June 2023). DOI: doi.org/10.1103/PhysRevLett.130.226003.

[12] S. Stringari. "Moment of Inertia and Superfluidity of a Trapped Bose Gas." In: *Phys. Rev. Lett.* 76 (9 Feb. 1996), pp. 1405–1408. DOI: 10.1103/PhysRevLett.76.1405.

[13] A. Filinov and Yu. Lozovik et al. "Path integral Monte Carlo results for Bose condensation of mesoscopic indirect excitons." In: *Solid State Physics* 3 (July 2006), pp. 2457–2460. DOI: doi.org/10.1002/pssc.200668038.

[14] Ahmed Hassan and A et al. Abdallah. "The superfluid fraction of ultracold interacting boson atoms trapped in a combined harmonic-deep optical potential." In: *Physics Letters A* 384 (Apr. 2020). DOI: 10.1016/j.physleta.2020.126476.

[15] Tommaso Macrì Matteo Ciardi and Fabio Cinti. "Finite-temperature phases of trapped bosons in a two-dimensional quasiperiodic potential." In: *Phys Rev A.* 105 (Jan. 2022). DOI: 10.1103/PhysRevA.105.L011301.

[16] Michael Fogler, L Butov, and K Novoselov. "High-temperature superfluidity with indirect excitons in van der Waals heterostructures." In: *Nature communications* 5 (July 2014), p. 4555. DOI: 10.1038/ncomms5555.

[17] Hongli Guo, Xu Zhang, and Gang Lu. "Tuning moiré excitons in Janus heterobilayers for high-temperature Bose-Einstein condensation." In: *Science Advances* 8.40 (2022), eabp9757. DOI: 10.1126/sciadv.abp9757.

[18] Kyle Seyler and Xiaodong et al. Xu. "Signatures of moiré-trapped valley excitons in MoSe2/WSe2 heterobilayers." In: *Nature* 567 (Mar. 2019). DOI: 10.1038/s41586-019-0957-1.

[19] Barak Hirshberg, Valerio Rizzi, and Michele Parrinello. "Path integral molecular dynamics for bosons." In: *Proceedings of the National Academy of Sciences* 116 (Oct. 2019), p. 201913365. DOI: 10.1073/pnas.1913365116.

[20] Yotam Feldman and Barak Hirshberg. "Quadratic scaling bosonic path integral molecular dynamics." In: *The Journal of Chemical Physics* 159 (Oct. 2023). DOI: 10.1063/5.0173749.

[21] D. M. Ceperley. "Path integrals in the theory of condensed helium." In: *Rev. Mod. Phys.* 67 (2 Apr. 1995), pp. 279–355. DOI: 10.1103/RevModPhys.67.279.

[22] Thomas E. Markland and Michele Ceriotti. "Nuclear quantum effects enter the mainstream." In: *Nat. Rev. Chem.* 2.0109 (Feb. 2018). DOI: 10.1038/s41570-017-0109.

[23] Shinichi Miura and Susumu Okazaki. "Path integral molecular dynamics for Bose Einstein and Fermi Dirac statistics." In: *J. Chem. Phys.* 112.23 (June 2000), pp. 10116–10124. DOI: /10.1063/1.481652.

[24] Tobias Dornheim and Michael et al. Bonitz. "Path integral Monte Carlo simulation of degenerate electrons: Permutation-cycle properties." In: *The Journal of Chemical Physics* 151 (July 2019), p. 014108. DOI: 10.1063/1.5093171.

[25] Chang Woo Myung, Barak Hirshberg, and Michele Parrinello. "Prediction of a Supersolid Phase in High-Pressure Deuterium." In: *Phys. Rev. Lett.* 128 (4 Jan. 2022), p. 045301. DOI: 10.1103/PhysRevLett.128.045301.

[26] Astrakharchik G. et al. Golomedov A. "Composite Boson Description of a Low-Density Gas of Excitons." In: *J Low Temp Phys* 189 (Oct. 2017), pp. 300–311. DOI: doi.org/10.1007/s10909-017-1814-y.

[27] Mark E. Tuckerman. *Statistical Mechanics: Theory and Molecular Simulation.* Oxford, 2023. ISBN: 9780198825562.

[28] Richard P. Feynman and Albert R. Hibbs. *Quantum Mechanics and Path Integrals.* Dover Publications, 2010. ISBN: 9780486477220.

[29] Pierre-Nicholas Roy. "Microscopic molecular superfluid response: Theory and simulations." In: *Reports on progress in physics. Physical Society (Great Britain)* 77 (Mar. 2014), p. 046601. DOI: 10.1088/0034-4885/77/4/046601.

[30] Sean Pearson, Tao Pang, and Changfeng Chen. "Bose-Einstein condensation in two dimensions: A quantum Monte Carlo study." In: *Phys. Rev. A* 58 (6 Dec. 1998), pp. 4811–4815. DOI: 10.1103/PhysRevA.58.4811.

[31] Philippe Sindzingre and David M. et al. Ceperley. "Path-integral Monte Carlo study of low-temperature $^4$He clusters." In: *Phys. Rev. Lett.* 63 (15 Oct. 1989), pp. 1601–1604. DOI: 10.1103/PhysRevLett.63.1601.

[32] Slava Grebenev, Peter Toennies, and Andrei Vilesov. "Superfluidity Within a Small Helium-4 Cluster: The Microscopic Andronikashvili Experiment." In: *Science (New York, N.Y.)* 279 (Mar. 1998), pp. 2083–6. DOI: 10.1126/science.279.5359.2083.

[33] Tobias Dornheim and Yangqian Yan. "Abnormal quantum moment of inertia and structural properties of electrons in 2D and 3D quantum dots: an ab initio path-integral Monte Carlo study." In: *New Journal of Physics* 24 (Nov. 2022). DOI: 10.1088/1367-2630/ac9f29.

[34] A. P. Thompson et al. "LAMMPS - a flexible simulation tool for particle-based materials modeling at the atomic, meso, and continuum scales." In: *Comp. Phys. Comm.* 271 (2022), p. 108171. DOI: 10.1016/j.cpc.2021.108171.

[35] Tobias Dornheim. "Path-integral Monte Carlo simulations of quantum dipole systems in traps: Superfluidity, quantum statistics, and structural properties." In: *Phys. Rev. A* 102 (2 Aug. 2020), p. 023307. DOI: 10.1103/PhysRevA.102.023307.

[36] Zhao Y. Rong and Pieter Kuiper. "Electronic effects in scanning tunneling microscopy: Moiré pattern on a graphite surface." In: *Phys. Rev. B* 48 (23 Dec. 1993), pp. 17427–17431. DOI: 10.1103/PhysRevB.48.17427.

[37] R. M. Wilcox. "Exponential Operators and Parameter Differentiation in Quantum Physics." In: *J. Math. Phys.* 8 (1967), pp. 962–982. DOI: 10.1063/1.1705306.

[38]   Yunuo Xiong and Hongwei Xiong. "On the thermodynamic properties of fictitious identical particles and the application to fermion sign problem." In: *The Journal of Chemical Physics* 157 (Sept. 2022). DOI: `doi.org/10.1063/5.01060679`.

[39]   Wai Kui Wong. "Solving 2D Time Independent Schrodinger Equation Using Numerical Method." In: (Dec. 2021). DOI: `10.13140/RG.2.2.12835.99360`.

# 6  Appendix

## 6.1  Appendix A - derivation of the superfluid fraction estimator

This derivation is an extent of a derivation made by [29].

The overall goal is to evaluate the superfluid fraction in the canonical ensemble denoted in Eq. 16. To determine $I_q$, we apply linear response theory, evaluating it in the following way,

$$I_q = \frac{\partial \langle \hat{L}_z \rangle}{\partial \omega_0} |_{\omega_0 = 0} \tag{26}$$

where $\hat{L}_z$ is the total angular momentum operator of the bosons along the $\hat{z}$ direction and $\langle ... \rangle$ stands for the thermal average. This derivative quantifies the linear response of the bosons to a rotational field characterized by an infinitesimally small angular velocity $\omega_0$ along the $z$ direction. The quantum moment of inertia should be evaluated in the rotating frame of reference (denoted in equations with a $'$) since Andronikashvili's experiment measures the contribution from the liquid to the rotor, nevertheless it can be shown that in the limit of $\omega_0 \to 0$ the Hamiltonians are equivalent ($\hat{H}' = \hat{H} - \omega_0 \hat{L}_z$) and the thermal averages can be taken in the fixed $\hat{z}$-axis frame

$$
\begin{aligned}
I_q &= \frac{\partial \langle \hat{L}_z \rangle}{\partial \omega_0} |_{\omega_0 = 0} \\
&= \frac{\partial}{\partial \omega_0} \frac{Tr(e^{-\beta \hat{H}'} \hat{L}_z)}{Z'} |_{\omega_0 = 0} \\
&= \frac{\partial}{\partial \omega_0} \frac{Tr(e^{-\beta \hat{H}'} \hat{L}_z)}{Tr(e^{-\beta \hat{H}'})} |_{\omega_0 = 0}
\end{aligned}
\tag{27}
$$

where $\hat{H}$ is the Hamiltonian operator in the fixed $\hat{z}$-axis reference frame. A known identity for the derivative of an exponential operator is [37]

$$
\begin{aligned}
\frac{\partial}{\partial \lambda} e^{-\beta \hat{H}} &= -\int_0^\beta e^{-(\beta - \tau)\hat{H}} \frac{\partial \hat{H}}{\partial \lambda} e^{-\tau \hat{H}} d\tau \\
\frac{\partial}{\partial \omega} e^{-\beta \hat{H}'} &= -\int_0^\beta e^{-(\beta - \tau)\hat{H}'} (-\hat{L}_z) e^{-\tau \hat{H}'} d\tau.
\end{aligned}
\tag{28}
$$

Since $\hat{L}_z$ does not depend on $\omega_0$, one can proceed by taking the derivative of the quotient,

$$I_q = \frac{\partial}{\partial \omega_0} \frac{Tr(e^{-\beta \hat{H}'} \hat{L}_z)}{Tr(e^{-\beta \hat{H}'})} |_{\omega_0 = 0} = \frac{Tr(\int_0^\beta e^{-(\beta - \tau)\hat{H}'} \hat{L}_z e^{-\tau \hat{H}'} \hat{L}_z d\tau)}{Z'} |_{\omega_0 = 0} - \frac{Tr(\int_0^\beta e^{-(\beta - \tau)\hat{H}'} \hat{L}_z e^{-\tau \hat{H}'}) d\tau Tr(e^{-\beta \hat{H}'} \hat{L}_z)}{Z'^2} |_{\omega_0 = 0}. \tag{29}$$

Since the trace operation is cyclic invariant and commutes with the integration, the right term can then be written as,

$$\frac{\int_0^\beta Tr(\overbrace{e^{-\tau \hat{H}'} e^{\tau \hat{H}'}}^{1} e^{-\beta \hat{H}'} \hat{L}_z) d\tau Tr(e^{-\beta \hat{H}'} \hat{L}_z)}{Z'^2} = \frac{\int_0^\beta d\tau Tr(e^{-\beta \hat{H}'} \hat{L}_z) Tr(e^{-\beta \hat{H}'} \hat{L}_z)}{Z'^2} = \beta \left( \frac{Tr(e^{-\beta \hat{H}'} \hat{L}_z)}{Z'} \right)^2 = \beta \langle \hat{L}_z \rangle^2 \tag{30}$$

where $\int_0^\beta d\tau = \beta$. The left term can be written as,

$$\frac{Tr(\int_0^\beta e^{-(\beta-\tau)\hat{H}'}\hat{L}_z e^{-\tau\hat{H}'}\hat{L}_z)d\tau}{Z'} = \frac{\int_0^\beta (Tr(e^{-\beta\hat{H}'}\overbrace{e^{\tau\hat{H}'}\hat{L}_z e^{-\tau\hat{H}'}}^{\hat{L}_z(\tau)}\hat{L}_z d\tau}{Z'} = \frac{\int_0^\beta (Tr(e^{-\beta\hat{H}'}\hat{L}_z(\tau)\hat{L}_z)d\tau}{Z'} = \int_0^\beta \langle\hat{L}_z(\tau)\hat{L}_z\rangle d\tau \tag{31}$$

where $\hat{L}_z(\tau)$ is the angular momentum operator in the Heisenberg picture. Then, the expression is simplified to

$$I_q = \int_0^\beta \langle\hat{L}_z(\tau)\hat{L}_z\rangle d\tau - \beta\langle\hat{L}_z\rangle^2. \tag{32}$$

In the limit as $\omega_0 \to 0$, the thermal averages can be computed within the fixed $\hat{z}$-axis reference frame using the Boltzmann operator, $e^{-\beta\hat{H}}$. In the case when the system exhibits time-reversal symmetry, it can be demonstrated that $\langle\hat{L}_z\rangle = 0$. This ultimately simplifies the expression to

$$I_q = \int_0^\beta \langle\hat{L}_z(\tau)\hat{L}_z\rangle d\tau. \tag{33}$$

Eq. 33 represents the angular momentum correlation function. If the bosons in the fluid adiabatically follow the rotation of the system their total angular momentum is maximally correlated. Conversely, at temperatures below the critical temperature, the bosons enter a superfluid state and remain unaffected by the rotating system. Consequently, their total angular momentum becomes zero, as it is randomly distributed. This results in a negligible quantum moment of inertia.

Practically, in order to calculate the superfluid fraction for finite systems, one needs to sample the area estimator [31]. The area estimator is derived by discretizing the integral in Eq. 33 into a sum and invoking the Trotter factorization as expressed in Eq. 34,

$$I_q = \int_0^\beta \langle\hat{L}_z(\tau)\hat{L}_z\rangle d\tau = \frac{\int_0^\beta (Tr(e^{-\beta\hat{H}}\hat{L}_z(\tau)\hat{L}_z)d\tau}{Z} = \frac{\int_0^\beta (Tr(e^{-(\beta-\tau)\hat{H}}\hat{L}_z e^{-\tau\hat{H}}\hat{L}_z)d\tau}{Z} \tag{34}$$

$$= \frac{\Delta\tau}{Z}Tr\sum_{k=1}^M e^{-(M-k)\Delta\tau\hat{H}}\hat{L}_z e^{-k\Delta\tau\hat{H}}\hat{L}_z = \frac{\Delta\tau}{Z}Tr(e^{-M\Delta\tau\hat{H}}\hat{L}_z^2 + \sum_{k=1}^{M-1} e^{-k\hat{H}\Delta\tau}\hat{L}_z e^{-(M-k)\hat{H}\Delta\tau}\hat{L}_z)$$

$$= \frac{\Delta\tau}{Z}Tr(e^{-M\Delta\tau\hat{H}}\hat{L}_z^2) + \frac{\Delta\tau}{Z}Tr(\sum_{k=2}^M \hat{L}_z e^{-(k-1)\hat{H}\Delta\tau}\hat{L}_z e^{-(M-k+1)\hat{H}\Delta\tau})$$

where $\beta = M\Delta\tau$, the integral is discretized by letting $\tau = k\Delta\tau$ for $k \in \mathbb{N}$, and in the third line, a variable change to $k+1$ is introduced. Additionally, the cyclic invariance and a linear mapping of the trace is used. To simplify the derivation, we substitute the familiar $\tau$ as the imaginary time interval in place of $\Delta\tau$,

$$I_q = \frac{\tau}{Z}Tr(e^{-M\tau\hat{H}}\hat{L}_z^2) + \frac{\tau}{Z}\sum_{k=2}^M Tr(\hat{L}_z e^{-(k-1)\hat{H}\tau}\hat{L}_z e^{-(M-k+1)\hat{H}\tau}). \tag{35}$$

For clarification and simplicity, $R_j$ subscript represents the imaginary time slice or bead of all $N$ particles. Lets look at the second trace term and write it in the position basis,

$$Tr(\hat{L}_z e^{-(k-1)\hat{H}\tau}\hat{L}_z e^{-(M-k+1)\hat{H}\tau}) = \int \langle R|\hat{L}_z e^{-(k-1)\hat{H}\tau}\hat{L}_z e^{-(M-k+1)\hat{H}\tau}|R\rangle dR \tag{36}$$

$$= \overbrace{\int}^{M\times integrals} dRdR_1...dR_{M-1}\langle R|\hat{L}_z e^{-\hat{H}\tau}|R_1\rangle\langle R_1|... \tag{37}$$

$$...\langle R_{k-2}|e^{-\tau\hat{H}}|R_{k-1}\rangle\langle R_{k-1}|\hat{L}_z e^{-\hat{H}\tau}|R_k\rangle\langle R_k|...e^{-\tau\hat{H}}|R_{M-1}\rangle\langle R_{M-1}|e^{-\tau\hat{H}}|R\rangle.$$

The exponents were factorized into propagators with imaginary time $\tau$ and in between them an identity operator,

$\int dR|R\rangle\langle R|$. The matrix element $\langle R|e^{-\tau\hat{H}}|R'\rangle$ represents the connection of one imaginary time slice or bead to the next of all $N$ particles as expressed in Eq. 3 and 4. The matrix element $\langle R|\hat{L}_z e^{-\tau\hat{H}}|R'\rangle$ can be generalized and expressed as,

$$\langle R|\hat{L}_z e^{-\tau\hat{H}}|R'\rangle = (-i\hbar)\sum_{i=1}^{N}(x_i\frac{\partial}{\partial y_i} - y_i\frac{\partial}{\partial x_i})\langle R|e^{-\tau\hat{H}}|R'\rangle. \tag{38}$$

This is because $\hat{L}_z$ is composed of position operators acting on the position eigenvector. From Eq. 3, 4 and 5 one understands that a matrix element of the Boltzmann factor is denoted as,

$$\langle R|e^{-\tau\hat{H}}|R'\rangle = \overbrace{(\frac{mP}{2\pi\beta\hbar^2})^{\frac{dN}{2}}}^{\equiv\lambda^{-dN}} e^{-\beta\sum_{l=1}^{N}\frac{1}{2}m\omega_P^2(r_l'-r_l)^2 + \frac{1}{P}U(r_1',...,r_N')}. \tag{39}$$

Invoking the Trotter factorization on the position representation of $\hat{L}_z$ yields,

$$\langle R|\hat{L}_z e^{-\tau\hat{H}}|R'\rangle = (-i\hbar)(-\frac{2\pi}{\lambda^2})\sum_{i=1}^{N}\overbrace{(x_i(y_i-y_i')-y_i(x_i-x_i'))}^{y_i x_i'-x_i y_i'=-(r_i\times r_i')_z} \times \overbrace{\lambda^{-dN}e^{-\beta\sum_{l=1}^{N}\frac{1}{2}m\omega_P^2(r_l'-r_l)^2+\frac{1}{P}U(r_1',...,r_N')}}^{\langle R|e^{-\tau\hat{H}}|R'\rangle} = \tag{40}$$

$$= (-i\hbar)(-\frac{2\pi}{\lambda^2})\sum_{i=1}^{N}-(r_i\times r_i')_z\langle R|e^{-\tau\hat{H}}|R'\rangle.$$

More specifically, the two terms involving $\hat{L}_z$ in Eq. 36 are,

$$\langle R|\hat{L}_z e^{-\tau\hat{H}}|R_1\rangle = (-i\hbar)(-\frac{2\pi}{\lambda^2})\sum_{i=1}^{N}-(r_i\times r_i^1)_z\langle R|e^{-\tau\hat{H}}|R_1\rangle = (-i\hbar)(\frac{4\pi}{\lambda^2})A_{1,z}\langle R|e^{-\tau\hat{H}}|R_1\rangle \tag{41}$$

$$\langle R_{k-1}|\hat{L}_z e^{-\tau\hat{H}}|R_k\rangle = (-i\hbar)(-\frac{2\pi}{\lambda^2})\sum_{i=1}^{N}-(r_i^{k-1}\times r_i^k)_z\langle R_{k-1}|e^{-\tau\hat{H}}|R_k\rangle = (-i\hbar)(\frac{4\pi}{\lambda^2})A_{k,z}\langle R_{k-1}|e^{-\tau\hat{H}}|R_k\rangle$$

where the subscript index represents the particle and the superscript represents the specific bead. The vector area between two adjacent beads of all $i$ particles is denoted as

$$A_k = \sum_{i=1}^{N}\frac{1}{2}(r_i^{k-1}\times r_i^k). \tag{42}$$

Inserting Eq. 41 into Eq. 36 and normalizing it with the partition function provides the following expression

$$\frac{1}{Z}Tr(\hat{L}_z e^{-(k-1)\hat{H}\tau}\hat{L}_z e^{-(M-(k-1))\hat{H}\tau}) = (-i\hbar)^2(\frac{4\pi}{\lambda^2})^2\langle A_{1,z}A_{k,z}\rangle, \tag{43}$$

therefore, the second term in Eq. 35 becomes,

$$\frac{\tau}{Z}\sum_{k=2}^{M}Tr(\hat{L}_z e^{-(k-1)\hat{H}\tau}\hat{L}_z e^{-(M-(k+1))\hat{H}\tau}) = \tau(-i\hbar)^2(\frac{4\pi}{\lambda^2})^2\sum_{k=2}^{M}\langle A_{1,z}A_{k,z}\rangle \tag{44}$$

$$= \tau(-i\hbar)^2(\frac{4\pi}{\lambda^2})^2(\langle A_{1,z}\sum_{k=1}^{M}A_{k,z}\rangle - \langle A_{1,z}A_{1,z}\rangle).$$

On the first term in Eq. 35 the same procedure can be applied,

$$\frac{\tau}{Z}Tr(e^{-M\tau\hat{H}}\hat{L}_z^2) = \overbrace{\int}^{M\times integrals} dRdR_1...dR_M\langle R|e^{-\hat{H}\tau}\hat{L}_z^2|R_1\rangle\langle R_1|...\langle R_{M-1}|e^{-\tau\hat{H}}|R\rangle. \tag{45}$$

Similarly to the derivation of the matrix element containing the $\hat{L}_z$ operator, lets further derive the matrix element

containing $\hat{L}_z^2$ by writing the operator twice in the position representation,

$$\langle R|\hat{L}_z^2 e^{-\tau\hat{H}}|R_1\rangle = (-i\hbar)^2 \sum_{j=1}^{N}(x_j\frac{\partial}{\partial y_j} - y_j\frac{\partial}{\partial x_j}) \sum_{i=1}^{N}(x_i\frac{\partial}{\partial y_i} - y_i\frac{\partial}{\partial x_i})\langle R|e^{-\tau\hat{H}}|R_1\rangle. \tag{46}$$

Inserting the matrix element $\langle R|e^{-\tau\hat{H}}|R_1\rangle$ and evaluating the derivative term involving the $i$ index,

$$= (-i\hbar)^2(-\frac{2\pi}{\lambda^2}) \sum_{j=1}^{N}\sum_{i=1}^{N}(x_j\frac{\partial}{\partial y_j} - y_j\frac{\partial}{\partial x_j})(y_i x_i^1 - x_i y_i^1)\lambda^{-dN} e^{-\beta\sum_{l=1}^{N}\frac{1}{2}m\omega_P^2(r_l^1 - r_l)^2 + \frac{1}{P}U(r_1^1,...,r_N^1)}. \tag{47}$$

The next step is to do the derivatives with respect to $y_j$ and $x_j$. This entails straightforward algebraic manipulations ultimately yielding,

$$(-i\hbar)^2(-\frac{2\pi}{\lambda^2})\langle R|e^{-\tau\hat{H}}|R_1\rangle \sum_{j=1}^{N}\sum_{i=1}^{N}(\delta_{i,j}(x_j x_i^1 + y_j y_i^1) + (-\frac{2\pi}{\lambda^2})(y_i x_i^1 - x_i y_i^1)(-x_j y_j^1 + y_j x_j^1)) \tag{48}$$

$$= (-i\hbar)^2(-\frac{2\pi}{\lambda^2})\langle R|e^{-\tau\hat{H}}|R_1\rangle \sum_{i=1}^{N}((x_i x_i^1 + y_i y_i^1) + (-\frac{2\pi}{\lambda^2})\overbrace{\sum_{i=1}^{N}(y_i x_i^1 - x_i y_i^1)}^{-2A_{1,z}}\overbrace{\sum_{j=1}^{N}(-x_j y_j^1 + y_j x_j^1)}^{-2A_{1,z}})$$

$$= (-i\hbar)^2(-\frac{2\pi}{\lambda^2})\langle R|e^{-\tau\hat{H}}|R_1\rangle[\sum_{i=1}^{N}((x_i x_i^1 + y_i y_i^1) + (-\frac{8\pi}{\lambda^2})A_{1,z}^2].$$

Therefore, when inserting the result of Eq. 48 in the first term on Eq. 35 one obtains

$$\frac{\tau}{Z}Tr(e^{-M\tau\hat{H}}\hat{L}_z^2) = \tau(-i\hbar)^2(-\frac{2\pi}{\lambda^2})\langle\sum_{i=1}^{N}(x_i x_i^1 + y_i y_i^1)\rangle + \tau(-i\hbar)^2(-\frac{16\pi^2}{\lambda^4}\langle A_{1,z}^2\rangle. \tag{49}$$

Finally, inserting Eq. 44 and 49 into Eq. 35 one can notice that the second summand cancels resulting in

$$I_q = \tau(-i\hbar)^2(-\frac{2\pi}{\lambda^2})\left[\langle\sum_{i=1}^{N}(x_i x_i^1 + y_i y_i^1)\rangle + (-\frac{8\pi}{\lambda^2})\langle A_{1,z}\sum_{k=1}^{M}A_{k,z}\rangle\right]. \tag{50}$$

In this derivation, the quantum moment of inertia is only evaluated when closed configurations are attained. Therefore, all beads should be treated as identical, making no distinction between the superscript "1" and any arbitrary superscript "$k$". This leads to further average over all beads. The first term of Eq. 50 then becomes

$$\langle\sum_{i=1}^{N}(x_i x_i^1 + y_i y_i^1)\rangle = \langle\sum_{i=1}^{N}(\hat{z}\times r_i)\cdot(\hat{z}\times r_i^1)\rangle = \frac{1}{M}\sum_{k=1}^{M}\langle\sum_{i=1}^{N}(\hat{z}^{k-1}\times r_i^{k-1})\cdot(\hat{z}^{k-1}\times r_i^k)\rangle \tag{51}$$

and the second term is

$$\langle A_{1,z}\sum_{k=1}^{M}A_{k,z}\rangle = \frac{1}{M}\sum_{k'=1}^{M}\langle A_{1,z}\sum_{k=1}^{M}A_{k,z}\rangle = \frac{1}{M}\langle\sum_{k'=1}^{M}A_{k',z}\sum_{k=1}^{M}A_{k,z}\rangle = \frac{1}{M}\langle(\sum_{k=1}^{M}A_{k,z})^2\rangle = \frac{1}{M}\langle A_z^2\rangle \tag{52}$$

where the total area is denoted as $A_z = \sum_{k=1}^{M}A_{k,z}$. The area estimator, $A_z$, is the total vector area of all the path or beads for all closed configurations. Substituting Eq. 51 and 52 into 50 and expressing $\lambda$ provides the final equation

for the quantum moment of inertia,

$$I_q = \frac{m}{M} \sum_{k=1}^{M} \langle \sum_{i=1}^{N} (\hat{z}^{k-1} \times r_i^{k-1}) \cdot (\hat{z}^{k-1} \times r_i^{k}) \rangle - \frac{4m^2}{\hbar^2 \beta} \langle A_z^2 \rangle = \tag{53}$$

$$= \frac{1}{M} m \sum_{i=1}^{N} \sum_{k=1}^{M} (r_i^{k,\perp} \cdot r_i^{k+1,\perp}) - \frac{4m^2}{\hbar^2 \beta} \langle A_z^2 \rangle$$

$$= \langle I_{cl} \rangle - \frac{4m^2}{\hbar^2 \beta} \langle A_z^2 \rangle.$$

Eq. 53 is used in molecular dynamics and Monte Carlo simulations. Now it becomes clearer why in Eq. 34 the sum is separated into two parts, the classical moment of inertia comes from the first term and the quantum reduction to the moment of inertia comes from the second term. The quantum reduction moment of inertia underlies the non-classical inertial response to the rotation of the system. Now, one can calculate the superfluid fraction using Eq. 16 along the $\hat{z}$-axis

$$\gamma_{sf} = \frac{4m^2 \langle A_z^2 \rangle}{\hbar^2 \beta \langle I_{cl} \rangle}. \tag{54}$$

It is important to notice that Eq. 54 is derived for distinguishable particles, nevertheless it is directly applicable to bosons through efficient permutation sampling during the simulation [29].

## 6.2 Appendix B - analytical solution for superfluid fraction for ideal bosons in a harmonic trap

For ideal (non-interacting) boson systems in a harmonic trap, the superfluid fraction can be computed analytically [35]. This is done by computing the classical and quantum moment of inertia, denoted as,

$$I_q = \frac{2\hbar^2 \beta}{Z_B(N,\beta)} \sum_{k=1}^{N} [\Gamma_{N,\beta}^B(k) \frac{k^2 e^{-k\beta\hbar\omega}}{(1 - e^{-k\beta\hbar\omega})^2}] \qquad\qquad I_{cl} = \frac{1}{Z_B(N,\beta)} \frac{\hbar}{\omega} \sum_{k=1}^{N} [\Gamma_{N,\beta}^B(k) k \frac{1 + e^{-k\beta\hbar\omega}}{1 - e^{-k\beta\hbar\omega}}] \tag{55}$$

where $\Gamma$ is the ancilla function denoted as,

$$\Gamma_{N,\beta}^B(k) = \sum_{\{C_k\}_r} C_k \prod_{r=1}^{N} \frac{Z_B(1, r\beta)^{C_r}}{C_r! r^{C_r}}. \tag{56}$$

and inserted in Eq. 16. In Eq. 56, $Z^B(N, \beta)$ is the non-interacting partition function for $N$ bosons under a harmonic trap at inverse temperature $\beta$ and $\{C_k\}$ denotes the set of all permutation cycles [35]. For example, for $N = 3$ bosons there are $N! = 6$ possible permutations, i.e.,

$$\{ \underbrace{123}_{\substack{(1)(2)(3) \\ C_1=3 \\ C_2=C_3=0}} , \underbrace{132}_{\substack{(1)(23) \\ C_1=C_2=1 \\ C_3=0}} , \underbrace{213}_{\substack{(12)(3) \\ C_1=C_2=1 \\ C_3=0}} , \underbrace{321}_{\substack{(13)(2) \\ C_1=C_2=1 \\ C_3=0}} , \underbrace{231}_{\substack{(123) \\ C_1=C_2=0 \\ C_3=1}} , \underbrace{312}_{\substack{(132) \\ C_1=C_2=0 \\ C_3=1}} \} \qquad\qquad \{C_k\} = \{[3,0,0],[1,1,0],[0,0,1]\} \tag{57}$$

where $C_k$ is the number of cycles of length $k$ within a specific permutation. This solution is used to benchmark the superfluid fraction results obtained from PIMD-B simulations of ideal bosons confined in a harmonic trap.

### 6.2.1 scaling law

To obtain the analytical scaling law presented in the results section, let's start by dividing only the prefactors of both the quantum and classical moments of inertia. We obtain the following relation,

$$\frac{I_q}{I_{cl}} \sim \frac{\frac{2\hbar^2\beta}{Z^B(N,\beta)}}{\frac{1}{Z^B(N,\beta)}\frac{\hbar}{\omega}} = 2\beta\hbar\omega = 2\frac{1}{k_BT}\sqrt{\frac{16\pi^2\hbar^2}{ma_m^2}}\sqrt{V} \tag{58}$$

where the right expression comes from inserting the value for $\hbar\omega = \sqrt{\frac{16\pi^2\hbar^2V}{ma_m^2}}$ from Eq. 22. The summand that includes the ancilla function in both the quantum and classical moment of inertia provides a constant. Thus, the temperature at half the superfluid fraction yields the following scaling law: $T \sim \sqrt{V}$ as presented in Fig. 11.

## 6.3 Appendix C - numerical stability in PIMD-B simulations

The numerical stability of Eq. 15 may suffer due to the presence of exponentially small numbers. Since $E_N^{(k)}$ is non-negative and its value increases with $k$, some of the $N$ exponent terms become extremely small. Consequently, the potential is evaluated using the expression:

$$V_B^{(N)} = \tilde{E} - \frac{1}{\beta}\Big[\ln\frac{1}{N}\sum_{k=1}^{N}e^{-\beta(E_N^{(k)}+V_B^{(N-k)}-\tilde{E})}\Big]. \tag{59}$$

The outcome is unaffected by the choice of $\tilde{E}$; however, it is selected to enhance numerical stability. An approach ensuring numerical stability for computing the potential is by choosing $\tilde{E}$ to be $\tilde{E} = \max_k[E_N^{(k)} + V_B^{(N-k)}]$. An analogous approach is employed in the equations utilized for computing the forces [19, 38].

## 6.4 Appendix D - recurrence relation for the total internal energy for 2D harmonic potential

For non-interacting particles subjected to a harmonic potential, one may employ the recurrence relation for the partition function of $N$ non-interacting bosons, expressed as $Z_B^{(N)} = \sum_{k=1}^{N} z_k Z_B^{(N-k)}$, where $z_k$ represents the partition function of a single-particle in a harmonic trap evaluated at the inverse temperature $k\beta$. With knowledge of the partition function, one can utilize Eq. 8 to compute the total energy as a function of temperature.

The implementation of the recurrence relation is shown in the following Python code:

```python
def getZk(k, bhw, dim):
    return np.power((np.exp(0.5 * k * bhw) / (np.exp(k * bhw) - 1)), dim)
def getdZk(k, bhw, dim):
    return -0.5 * k * dim * getZk(k, bhw, dim) * (1 + np.exp(-k * bhw)) \\
    / (1 - np.exp(-k * bhw))
def get_harmonic_energy(n, bhw, dim, is_bosonic=True):
    if not is_bosonic:
        return -n * getdZk(1, bhw, dim) / getZk(1, bhw, dim)
    z_arr = np.zeros(n + 1)
    dz_arr = np.zeros(n + 1)
    z_arr[0] = 1.0
    for m in range(1, n + 1):
        sig_z = 0.0
        sig_dz = 0.0
        for j in range(m, 0, -1):
            sig_z += getZk(j, bhw, dim) * z_arr[m - j]
            sig_dz += getdZk(j, bhw, dim) * z_arr[m - j] + \\
```
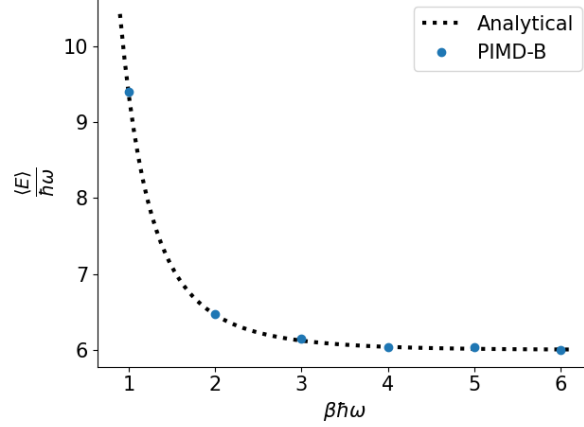
```
        + getZk(j, bhw, dim) * dz_arr[m − j]
    z_arr[m] = sig_z / m
    dz_arr[m] = sig_dz / m

return −dz_arr[n] / z_arr[n]
```

This codes is tested for $N = 6$ ideal bosons in a harmonic trap and compared to PIMD-B simulation results as shown in Fig. 15. The number of beads used for the PIMD-B simulations is $P = 64, 64, 48, 48, 32$, and 16 at inverse temperatures of $\beta\hbar\omega = 6, 5, 4, 3, 2$, and 1, respectively.



**Figure 15:** The total energy of the system is plotted against inverse temperatures. The analytical solution is presented by the black dashed line, while the blue data points represent the PIMD-B results. The energy in PIMD-B is evaluated using the virial estimator.

## 6.5   Appendix E - solving numerically the 2D time-independent Schrodinger equation

In order to tune the anharmonic strength parameter to match the harmonic fundamental energy, we solved the single-particle 2D time-independent Schrodinger equation [39]. This method was employed to tune the anharmonic strength parameters outlined in Table 1. All anharmonic simulations utilized the following parameters: $L = 300$, $n = 75$, $m = 0.84$.

```
def laplacian_1D(n):
    D = −2.0 * np.eye(n)
    for i in range(n−1):
        D[i, i+1] = D[i+1, i] = 1
    return D
def laplacian_2D(n):
    D1 = laplacian_1D(n)
    return np.kron(D1, np.eye(n)) + np.kron(np.eye(n), D1)
def two_d_schrodinger(L, n, s, pot):
    '''
    :param L: length of X and Y coordinates
    :param n: dimension of matrix
    :param s: number of energy state wanted to be outputed
    :param pot: string. either "harm" or "anharm"
    :return: eigenvalues, eigenvector
    '''
    x = np.linspace(−L, L, n)
    dx = x[1] − x[0]
```

```
    X = np.kron(x, np.ones(n))
    Y = np.kron(np.ones(n), x)
    if pot == 'harm':
1.36831859*10**-6, 8.10542107*10**-7, 3.97972642*10**-7
        k = 8.10542107*10**-7   # Change k accordingly, Units: [Hartree/bohr**2]
        V = np.diag(0.5 * k * (X ** 2 + Y ** 2))
    elif pot == 'anharm':
        l = 3.28*10**-11   # Change l accordingly, Units: [Hartree/bohr**4]
        V = np.diag(l * (X**4 + Y**4) + 2*l*((X**2)*(Y**2)))
    T = -hbar ** 2 / (2 * m) / (dx ** 2) * laplacian_2D(n)
    H = T + V
    # Eigenvalues and Vectors
    E, U = np.linalg.eigh(H)
    psi = U[:, s].reshape(n, n)


    return E, psi
```

## 6.6  Appendix F - python code that identifies the most probable permutation in PIMD-B

The Python code that returns the most probable permutation per time-step, $t$ is presented below. The input parameters: natoms, beads, t, and dorb represent the number of atoms, a tuple ordered as follows: (number of beads, all the data points, number of atoms, atom's (x,y,z) coordinates), MD time-step, and Boolean for Bosonic simulations, respectively. The code returns a list of the most probable permutation per MD time-step.

```
def permutations_pimd(natoms, beads, t, dorb=True):
    if dorb==True:   # For Bosonic simulations (dorb=True)
        ring_dist = []
        pair = []
        for i in range(natoms):   # natoms
            delR = beads[0, t, :, :] - beads[-1, t, i, :]
            j = LA.norm(delR, axis=-1).argmin()
            if (i != j):
                pair += [(i, j)]   # Which particle is connected to which
            else:
                ring_dist += [1]
            for e in range(len(pair) - 1):
                if j == pair[e][1]:
                    pair.pop(-1)
        g_connected, ring_len_dist, G = to_graph_jacob(pair)
        ring_dist += ring_len_dist
        # Adds Single configurations (that are not part of any other configuration)
        g_connected1 = list(flatten(g_connected))
        for i in range(natoms):
            if i not in g_connected1:
                g_connected += [[i]]
    else:  # For distinguishable simulations (dorb=False)
        g_connected = [[i] for i in range(natoms)]
    return g_connected
```

# תקציר

מוליכים למחצה דו-שכבתיים מסובבים מהווים פלטפורמה טובה לחקר התעבות בוז-איינשטיין של אקסיטונים בטמפרטורות גבוהות.  בשל יציבותם הגבוהה, וזמני החיים הארוכים של אקסיטונים בחומרים אלו, קיים סיכוי מוגבר להתעבותם בטמפרטורות גבוהות.  כדי לחקור תופעה זו, השתמשנו בדינמיקה מולקולרית לדגימה של פונקציית החלוקה הקוונטית המיוצגת על ידי אינטגרל מסלול. שיטה זו מאפשרת חישוב של תכונות תרמודינמיות של מערכות קוונטיות בשיווי משקל, ובפרט עבור בוזונים. בעבודה זו, הטמענו אלגוריתם לחישוב שבר העל-נוזל כמדד לטמפרטורת העיבוי.  לאחר מכן, חקרנו את ההשפעות של פרמטרים שונים בחומרים אלו על טמפרטורת העיבוי: מידת האנהרמוניות, עומק הקשר וזווית הסיבוב. תוצאות הסימולציה שלנו מראות כי לאנהרמוניות תפקיד מרכזי בהשפעה על טמפרטורת העיבוי, ולכן יש לקחת אותה בחשבון במודלים חישוביים לחומרים דו שכבתיים מסובבים. כמו כן, אנו רואים שככל שעומק הקשר גדול יותר וזווית הסיבוב גדולה יותר, שבר העל-נוזל גבוה יותר. הממצאים מספקים תובנות חשובות לתכנון של ניסויים עתידיים בעלי פוטנציאל לגילוי עיבוי של אקסיטונים בטמפרטורות גבוהות בחומרים דו-שכבתיים מסובבים.

**הפקולטה למדעים**
**מדויקים ע"ש ריימונד**
**ובברלי סאקלר**
אוניברסיטת תל אביב
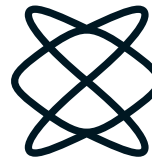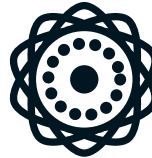
בית הספר לכימיה

# סימולציות של התעבות אקסיטונים
# בחומרים דו-שכבתיים מסובבים

חיבור זה הוגש כחלק מהדרישות לקבלת
התואר השני באוניברסיטת תל אביב

על ידי
**נתנאל בכר שוורץ**

העבודה הוכנה בהדרכתו של
**דר׳ ברק הירשברג**